

Comparing 1-year GUMICS–4 simulations of the Terrestrial Magnetosphere with Cluster Measurements

G. Facskó^{1,2,3}, D. G. Sibeck², I. Honkonen⁴, L. Degener^{4*}, P. Peitso^{5†},
E. I. Tanskanen⁵, C. R. Anekallu⁶, J. Kalmár⁷, J. Bór⁷, G. Farinas Perez^{2,3‡},
S. Szalai⁷, Á. Kis⁷, V. Wesztergom⁷

¹Wigner Research Centre for Physics, Budapest, Hungary

²NASA Goddard Space Flight Center, Greenbelt, Maryland, USA

³the Catholic University of America, Washington DC, USA

⁴Finnish Meteorological Institute, Helsinki, Finland

⁵Aalto University, School of Electrical Engineering, Espoo, Finland

⁶UCL Department of Space & Climate Physics, Mullard Space Science Laboratory, Dorking, UK

⁷Research Centre for Astronomy and Earth Sciences, Sopron, Hungary

Key Points:

- The GUMICS–4 provides realistic ion plasma moments and magnetic field in the solar wind and the outer magnetosheath.
- The code can predict the realistic location of the bow shock.
- An inner magnetosphere model should be added to the code to increase the accuracy of the simulation.

*Now private individual, Hannover, Germany

†Now at Aurora Propulsion Technologies, Espoo, Finland

‡Now at University of Miami, Electrical and Computer Engineering Department, Miami, Florida, USA

Corresponding author: Gábor Facskó, gabor.i.facsko@gmail.com

19 **Abstract**

20 Previously a 1-year global magnetohydrodynamics simulation was made using the GUMICS–4
 21 code and the OMNI 1-min resolution solar wind data from January 29, 2002 to Febru-
 22 ary 2, 2003 as input. The simulation data was saved along the orbit of the Cluster SC3
 23 reference spacecraft. We compare the saved parameters with the Cluster SC3 measure-
 24 ments. We use the magnetic field Z component, the solar wind velocity X component
 25 and the solar wind density of the Cluster magnetometer, ion plasma and spacecraft po-
 26 tential measurements geocentric solar ecliptic reference frame. We select intervals in the
 27 solar wind, the magnetosheath and the magnetosphere where the instruments above pro-
 28 vided good quality data and the spacecraft and the simulation are in the same region.
 29 We determine the location of the bow shock, the magnetopause and the neutral sheet
 30 in the spacecraft measurements and compare their position in the observation and sim-
 31 ulations.

32 The GUMICS–4 provides quite good results in the solar wind however its accu-
 33 racy is significantly worse in the magnetosheath. The simulation results are not realis-
 34 tic in the magnetosphere. The bow shock location is predicted well however the mag-
 35 netopause location is less accurate. The neutral sheet positions are located quite well
 36 thanks to the special solar wind conditions. The reason for these inaccuracies is the miss-
 37 ing inner magnetosphere model.

38 **1 Introduction**

39 The most cost-effective way to study the interaction of the solar wind and the plan-
 40 etary magnetospheres (or predict the conditions of the near-Earth space) is using a global
 41 magnetohydrodynamic (MHD) code. In the past, several robust, parallelized, effective,
 42 verified and validated codes were developed, which are used and applied to forecast the
 43 cosmic environment of the Earth; such as the Lyon-Fedder-Mobarry [LFM; *Lyon et al.*,
 44 2004] code, the Open Geospace General Circulation Model [OpenGGCM; *Raeder et al.*,
 45 2008], the Block-Adaptive-Tree-Solarwind-Roe-Upwind-Scheme [BATS-R-US; *Powell et al.*,
 46 1999; *Tóth et al.*, 2012]. In Europe only three global MHD codes were developed: the
 47 Grand Unified Magnetosphere–Ionosphere Coupling Simulation [GUMICS–4; *Janhunen*
 48 *et al.*, 2012], the Computational Object Oriented Libraries for Fluid Dynamics [COOLFluiD;
 49 *Lani et al.*, 2012] and the 3D resistive magnetohydrodynamic code Gorgon [*Chittenden*
 50 *et al.*, 2004; *Ciardì et al.*, 2007]. The COOLFluiD is a general-purpose plasma simula-

tion tool. The Gorgon code was developed for studying high energy, collisional plasma interactions and has been adapted to simulate planetary magnetospheres and their interaction with the solar wind [Mejnertsen *et al.*, 2016, 2018]. The GUMICS–4 was developed to study the solar wind-terrestrial magnetosphere interaction and its parallel version has not been available for the scientific community (see Section 2.1). These codes are available at the Community Coordinated Modelling Center (CCMC; <http://ccmc.gsfc.nasa.gov/>) hosted by the NASA Goddard Space Flight Center (GSFC) and the Virtual Space Weather Modelling Centre (VSWMC; <http://swe.ssa.esa.int/web/guest/kul-cmpa-federated>) hosted by the KU Leuven [Poedts *et al.*, 2020]. The comparison of the simulation results to space-craft and ground-based measurements is necessary to understand the abilities and features of the developed tools. The statistical study using long term global MHD runs for validation and verification of the codes seems to be a good and fruitful method. However, providing long simulations is costly and time consuming hence only a few studies were done previously using much shorter simulations than a year.

Guild et al. [2008a,b] launched two months of LFM run and compared the plasma sheet properties in the simulated tail with the statistical properties of six years Geotail magnetic field and plasma observations [Kokubun *et al.*, 1994; Mukai *et al.*, 1994]. The LFM successfully reproduced the global features of the global plasma sheet in statistical sense. However, there were some differences. The sheet was too cold, too dense and the bulk flow was faster than the observed plasma sheet. The LFM overestimated the ionospheric transpolar potential. The transpolar potential correlated with the speed of the plasma sheet flows. The equatorial maps of density, thermal pressure, thermal energy and velocity were compared. The LFM overestimated the plasma sheet density close to the Earth and underestimated the temperature by a factor of ~ 3 . The LFM overestimated the global average flow speed by a factor of ~ 2 . The LFM reproduced many of the climatological features of the Geotail data set. The low-resolution model underestimated the occurrence of the fast earthward and tailward flows. Increasing the simulation resolution resulted in the development of fast, busty flows. These flows contributed to the statistics and brought the simulations to the observations closer.

Zhang et al. [2011] launched a two months long LFM simulation to study the statistics of magnetosphere-ionosphere (MI) coupling. The LFM simulation was also used in the previous study of *Guild et al.* [2008a]. The polar cap potential and the field aligned currents (FAC), the downward Poynting flux and the vorticity of the ionospheric con-

84 convection were compared with observed statistical averages and the Weimer05 empirical
 85 model [Weimer, 2005]. The comparisons showed that the LFM model produced quite
 86 accurate average distributions of the Region 1 (R1) and Region 2 (R2) currents. The iono-
 87 spheric Region 2 currents in the MHD simulation seemed to be originated from the dia-
 88 magnetic ring current. The average LFM Region 1 and 2 currents were smaller compared
 89 with the values from the Weimer05 model. The average CPCP was higher in the LFM
 90 simulation than the measurements of the SuperDARN and the Weimer05 model. The
 91 average convention pattern was quite symmetric in the LFM simulation against the Su-
 92 perDARN measurements and the Weimer05 model. The SuperDARN measurements and
 93 the Weimer05 model had dawn-dusk asymmetry. In the LFM model more Poynting flux
 94 flowed into the polar region ionosphere than in the Weimer05 model. It was the conse-
 95 quence of the larger CPCP in the LFM simulation. The larger CPCP allowed higher elec-
 96 tric field in the polar region. The statistical dependence of the high-latitude convection
 97 patterns on Interplanetary Magnetic Field (IMF) clock angle was similar to the Super-
 98 DARN measurements [Sofko *et al.*, 1995] and the Weimer05 model. The average iono-
 99 spheric field-aligned vorticity showed good agreement on the dayside. However, the LFM
 100 model gave larger nightside vorticity than SuperDARN measurements because the Ped-
 101 ersen conductance on the night side ionosphere was too low.

102 *Wiltberger et al.* [2017] studied the structure of the high latitude field-aligned cur-
 103 rent patterns using three resolutions of the LFM global MHD code and the Weimer05
 104 empirical model [Weimer, 2005]. The studied period was a month long and contained
 105 two high-speed streams. Generally, the patterns agreed well with results obtained from
 106 the Weimer05 computing. As the resolution of the simulations increased, the currents be-
 107 came more intense and narrow. The ratio of the Region 1 (R1), the Region 2 (R2) cur-
 108 rents and the R1/R2 ratio increased when the simulation resolution increases. However,
 109 both the R1 and R2 currents were smaller than the predictions of the Weimer05 model.
 110 This effect led to a better agreement of the LFM simulation results with the Weimer 2005
 111 model results. The CPCP pattern became concentrated in higher latitudes because of
 112 the stronger R2 currents. The relationship of the CPCP and the R1 looked evident at
 113 higher resolution of the simulation. The LFM simulation could have reproduced the sta-
 114 tistical features of the field aligned current (FAC) patterns.

115 *Haducek et al.* [2017] simulated a month of January 2005 using the Space Weather
 116 Modelling Framework [SWMF; Tóth *et al.*, 2005] and the OMNI solar wind data as in-

117 put. The simulations were done with and without inner magnetosphere model and us-
 118 ing two different grid resolutions. The model was very good in predicting the currents
 119 circling the Earth around the dipole axis [SYM-H; <http://wdc.kugi.kyoto-u.ac.jp/aeasy/asy.pdf>;
 120 *Iyemori*, 1990]. The K_p index (that measures the general magnetospheric convention and
 121 the auroral currents [*Bartels et al.*, 1939; *Rostoker*, 1972; *Thomsen*, 2004]) was predicted
 122 well during storms however the index was over predicted during quiet time periods. The
 123 AL index (that describes the westward electro jet of the surface magnetic field introduced
 124 by *Davis and Sugiura* [1966]) was predicted reasonably well in average however the model
 125 reached the highest negative AL value less often than the observations because the model
 126 captured the structure of the auroral zone currents poorly. The overpredicting of K_p in-
 127 dex during quiet times might have had the same reason because that index was also sen-
 128 sitive for the auroral zone dynamics. The SWMF usually over predicted the CPCP. These
 129 results were not sensitive to grid resolutions. Except that the AL index reached the high-
 130 est negative value more often when the grid resolution was higher. Switching off of the
 131 inner magnetosphere model had dramatic effect for the accuracy of all quantities men-
 132 tioned above, except the CPCP.

133 In this paper the Cluster SC3 measurements are compared directly to a previously
 134 made 1-year long GUMICS–4 simulation in the solar wind, magnetosheath and the mag-
 135 netosphere along the Cluster SC3 orbit saved from the simulation results and measured
 136 by the spacecraft [*Facskó et al.*, 2016]. Three parameters (B_z , V_x and n) were studied
 137 as well as the location of the bow shock, magnetopause and the neutral sheet. The struc-
 138 ture of this paper is as follows. Section 2 describes the GUMICS–4 code, the 1-year sim-
 139 ulation and the instruments. Section 3 gives comparisons between the simulations and
 140 observations. Results of the comparison are discussed in Section 4. Finally, Section 5 con-
 141 tains the conclusions.

142 2 The GUMICS–4 products and Cluster measurements

143 Here we use two types of very different and difficult time series. The first type is
 144 derived from a previously made 1-year GUMICS–4 simulation [*Facskó et al.*, 2016]. The
 145 second type was measured by the magnetometer, ion plasma and electric field instruments
 146 of the Cluster reference spacecraft.

147 **2.1 The GUMICS–4 code**

148 The GUMICS–4 has two coupled simulation domains, the magnetospheric domain
 149 outside of $3.7 R_E$ radius around the Earth and a coupled ionosphere module containing
 150 a 3D electron density model of the ionosphere. The GUMICS–4 is not a parallel code
 151 however it was extensively used for studying the energy propagation processes from the
 152 solar wind to the magnetosphere through the magnetopause and other features [Janhunen
 153 *et al.*, 2012, see the references therein]. The code has also been applied for studying the
 154 forced reconnection in the tail [Vörös *et al.*, 2014]. Recently a few hundreds of synthetic
 155 two hours duration GUMICS–4 simulations were made to compare the simulation re-
 156 sults to empirical formulas [Gordeev *et al.*, 2013]. The agreement was quite good how-
 157 ever the diameter of the magnetopause deviated significantly in the simulation and the
 158 observations in the tail. The tail of the GUMICS–4 was smaller than spacecraft observed
 159 and measured. A 1-year long simulation was made using the GUMICS–4 code [Facskó
 160 *et al.*, 2016]. Juusola *et al.* [2014] compared the ionospheric currents, fields and the cross
 161 polar cap potential (CPCP) in the simulation versus Super Dual Auroral Radar Network
 162 (SuperDARN) radars [Greenwald *et al.*, 1995] and CHAMP spacecraft [Reigber *et al.*,
 163 2002] field aligned currents (FAC) measurements [Juusola *et al.*, 2007; Ritter *et al.*, 2004].
 164 The agreement was good in the seasonal variation of the CPCP however the FAC and
 165 other currents could not be reproduced properly. The possible cause of this bad agree-
 166 ment could be the lack of the inner magnetosphere model. This statement is supported
 167 by the result of Haiduček *et al.* [2017]. Haiduček *et al.* simulated only a month using dif-
 168 ferent spatial resolution and to test the codes switched off the inner magnetosphere model
 169 of the SWMF for a special run. This run without inner magnetosphere model made it
 170 clear that only the CPCP parameter of the simulation agreed quite well with the mea-
 171 surement. This fact explained why the agreement between the Cluster SC3 and the GUMICS-
 172 4 simulations was so good as described by [Lakka *et al.*, 2018a,b] based on the CPCP
 173 in GUMICS–4 simulations. Kallio and Facskó [2015] determined the solar wind param-
 174 eters along the Moon orbit using the results of the Facskó *et al.* [2016]’s global MHD sim-
 175 ulations. The solar wind parameters differed significantly in the geotail that should have
 176 been considered in future studies of the interaction of the solar wind and the lunar or-
 177 bit. Facskó *et al.* [2016] determined the footprint of the Cluster SC3 using the 1-year sim-
 178 ulation and the Tsyganenko T96 empirical model [Tsyganenko, 1995]. The code seemed
 179 to react slower to the dynamic changes of the solar wind pressure than the empirical model.

180 The agreement of the footprint is better in the Northern Hemisphere. The GUMICS-4
 181 tail looked shorter in the simulations than the observations. Finally, the Y component
 182 of the interplanetary magnetic field twisted the simulated tail hence the agreement of
 183 the empirical and computational footprints was worse at such solar wind conditions.

184 A workpackage of the European Cluster Assimilation Technology (ECLAT) project
 185 (https://cordis.europa.eu/result/rcn/165813_en.html; <http://www.eclat-project.eu/>) was
 186 the creation and analysis of a 1-year global MHD simulation using the OMNI solar wind
 187 data from January 29, 2002 to February 2, 2003 as input of the GUMICS-4 code [Facsikó
 188 *et al.*, 2016]. The GUMICS-4 was a single core system [Janhunen *et al.*, 2012] hence the
 189 1-year simulation was made in 1860 independent runs. This interval covered 155 Clus-
 190 ter SC3 orbits and each orbit lasted 57 hours. The supercomputer had 12 CPUs on each
 191 node hence the 57 hours were divided into 4.7 hours simulation time with one hour ini-
 192 tialisation period. Each sub-intervals used its own average Geocentric Solar Ecliptic (GSE)
 193 IMF magnetic field X component B_x component and dipole tilt angle. All data gaps of
 194 the input file were filled using interpolation. If the data gap of the input file was at the
 195 beginning (or the end) interval the first (or last) good data of the input file was used to
 196 fill the gap. The initialisation of each simulations was made using constant values. These
 197 values were the first valid data of the input file repeated 60 times (60 minutes) in the
 198 input file of the sub-interval. The simulation results were saved in every five minutes.
 199 Various simulation parameters, for example, the density, particle density, temperature,
 200 magnetic field, solar wind velocity (29 different quantities) were saved from the simu-
 201 lation results along the Cluster reference spacecraft in the GSE coordinates. In this pa-
 202 per these parameters, namely the B_z magnetic field GSE Z component, the solar wind
 203 velocity GSE X component (V_x) and the solar wind density n are compared to the Clus-
 204 ter SC3 measurement. These parameters are selected because the B_z controls the mag-
 205 netosphere, the V_x is the main solar wind velocity component and the n is the ion plasma
 206 momentum that is the easiest to calculate; furthermore more instruments could deter-
 207 mine it (see Section 2.2).

208 2.2 The Cluster SC3 measurements

209 The Cluster-II spacecraft of the European Space Agency (ESA) were launched in
 210 2000 and study the geospace since then [Credland *et al.*, 1997; Escoubet *et al.*, 2001]. Its
 211 four spacecraft form a tetrahedron however here we use only the measurements of the

reference spacecraft, the Cluster SC3. The spacecraft were stabilised by rotation and its period is ~ 4 s. Hence, the temporal resolution of the plasma instruments were considered 4 s and we use 4 s averaged magnetic field data. The real resolution of the Cluster FluxGate Magnetometer (FGM) magnetic field instrument was 27 Hz [Balogh *et al.*, 1997, 2001]. The ion plasma data was provided by the Cluster Ion Spectrometry (CIS) Hot Ion Analyser (HIA) sub-instrument [Reme *et al.*, 1997; Rème *et al.*, 2001]. The CIS HIA instrument is calibrated using the Waves of HIgh frequency Sounder for Probing the Electron density by Relaxation (WHISPER) wave instrument onboard Cluster [Décréau *et al.*, 2001; Trotignon *et al.*, 2010; Blagau *et al.*, 2013, 2014]. These calibrations might have appeared as sudden non-physical jumps in the CIS HIA data. The CIS HIA had different modes to measure in the solar wind and the magnetosphere. When the instrument switched from a mode to another mode it appeared as a non-physical jump in the measured data too. These features had an influence on the accuracy of the data analysis.

We protect our results from these non-physical jumps described previously using a density determination based on different principles. We use the spacecraft potential of the Electric Field and Wave Experiment [EFW ; Gustafsson *et al.*, 1997, 2001] to determine the electron density. This quantity can be calculated using the empirical density formula

$$n_{EFW} = 200(V_{sc})^{-1.85}, \quad (1)$$

where n_{EFW} is the calculated density and V_{sc} is the Cluster EFW spacecraft potential [Trotignon *et al.*, 2010, 2011]. The EFW and the WHISPER were used for the calibration of the CIS HIA and the Plasma Electron and Current Experiment [PEACE; Johnstone *et al.*, 1997; Fazakerley *et al.*, 2010a,b]. Both instruments were still working onboard all Cluster spacecraft. Their stable operation reduced the number of data gaps; furthermore made the data analysis easier.

3 Comparison of measurements to simulation

The saved parameters from the GUMICS–4 simulations and the Cluster SC3 magnetic field, solar wind velocity and density measurements are compared in the solar wind, magnetosheath and magnetosphere using cross correlation calculation. The resolution of the simulated Cluster orbit data is mostly five minutes because the simulations are saved in every five minutes [Facsikó *et al.*, 2016]. However, the time difference between points could be more than five minutes at the boundary of the subintervals, because the

length of simulation intervals is determined in minutes. To facilitate analysis of the simulation results, all simulation data were interpolated to one minute resolution. This method does not provide extra information to the cross correlation calculation. The data gaps are eliminated using interpolation in the data and extrapolation when the gap is at the start or the end of the selected interval. The spin resolution (4s) of Cluster SC3 magnetic field measurements is averaged over one minute around ($\pm 30\text{ s}$) the time stamps of the saved data.

For the correlation calculation intervals are selected carefully in the solar wind, the magnetosheath, the dayside and the night side magnetosphere. In these intervals the parameters did not vary a lot and neither the Cluster nor the virtual probe crossed any boundary layers. To compare the shape of the B_z magnetic field, V_x solar wind speed and the n_{CIS} and the n_{EFW} curves we calculate cross correlation on selected intervals. Sometimes we get very bad results. Then we carefully examined the case and remove the short intervals (shorter than four hours) from the correlation calculation and large data gaps from the correlation calculation. (The data gaps are interpolated however they cause loss of information.) Those intervals are also neglected where the plasma instrument has a calibration error or changes its mode from magnetosphere to solar wind (for example). The electron density is also calculated using the empirical density formula (see Equation 1) and making the correlation calculation. We want to avoid calibration errors and sudden non-physical jumps mentioned previously. The results do not differ significantly however the n_{EFW} does not have any mode change and it is applicable in the magnetosphere too (against the CIS HIA instrument).

3.1 Solar wind

We use OMNI IMF and solar wind velocity, density and temperature data as input of the simulation. Nevertheless, it is not useless to compare the solar wind region in the simulation and the measurements. The IMF X component cannot be given to the GUMICS–4 as input [Janhunen *et al.*, 2012; Fácskó *et al.*, 2016]. However the magnetic field of the solar wind has X component in the simulations. Additionally the solar wind structure might change from the simulation domain boundary at $+32 R_E$ to the sub-solar point of the terrestrial bow shock where all OMNI data is shifted. Almost the same solar wind intervals are used as in the see Table 1 of Fácskó *et al.* [2016]. The number of these intervals is small because the Cluster fleet instruments were calibrated in 2002, just

275 after launching (Table 1). Hence we do not have a satisfactory ion plasma data cover-
 276 age for this year. Additionally, to improve the accuracy of the correlation calculation (see
 277 below) we delete the intervals that were too short (shorter than five hours) or the CIS
 278 HIA instrument changed its mode. The Cluster fleet is located in the solar wind only
 279 from December to May and only for a couple of hours during each orbit near to the apogee.
 280 We double check whether the Cluster SC3 stays in the solar wind in both the simula-
 281 tion and reality. We also check the omnidirectional CIS HIA ion spectra on the Clus-
 282 ter Science Archive (CSA; <https://www.cosmos.esa.int/web/csa/csds-quicklook-plots>).
 283 Hence 17 intervals are left in the solar wind to study (Figure 1).

284 The selected intervals have quiet solar wind conditions (Figure 2). The GUMICS-4
 285 simulation results have five minutes resolution and the Cluster SC3 measurements have
 286 one minute resolution (Figure 3). The measurements vary significantly. In spite of the
 287 quiet conditions the solar wind density often changes and deviates from the simulation.
 288 On Figure 4c both densities deviate significantly. The CIS HIA density deviation is larger
 289 as it is expected because of the complexity and the large number of working modes of
 290 the CIS instrument. The magnetic field and the solar wind velocity fit better. On Fig-
 291 ure 5a the correlation of the magnetic field is very good; furthermore on Figure 5c, 5e, 5f
 292 the correlation of the solar wind velocity and density is excellent (Table 1). The time
 293 shift on Figure 5b, Figure 5d, Figure 5f is about five minutes for the magnetic field and
 294 the CIS data. On Figure 5h for the EFW data the time shift is worse. It is not deter-
 295 mined as well as the other parameters.

296 3.2 Magnetosheath

297 The Cluster SC3 spent only a little time in the solar wind from December, 2002
 298 to May, 2003. However, the orbit of the spacecraft always crosses the magnetosheath (Fig-
 299 ure 6). We selected intervals when the value of the magnetic field is around 25 nT. The
 300 field should be fluctuating because of the turbulent and deviated flow of the solar wind
 301 after passing the bow shock. In the same time the solar wind temperature increases. The
 302 solar wind speed drops hence its value is only 100-300 km/s. The density of the plasma
 303 flow increased and reached the $10\text{--}20 \text{ cm}^{-3}$. The narrow band on the omnidirectional CIS
 304 HIA ion spectra from the CSA (<https://www.cosmos.esa.int/web/csa/csds-quicklook->
 305 plots) is widened after passing the bow shock. 15–30 minutes after this crossing we con-
 306 sidered the Cluster SC3 to enter into the magnetosheath. At the inner boundary the flow

speed drops and the density as well. The magnetic field starts growing and it is less turbulent than in the magnetosheath. The wide band on the the omnidirectional CIS HIA ion spectra disappears. 15-30 minutes before the appearance of these indicators of the magnetopause crossing our intervals end. All intervals contain large data gap, non-physical jump of instrument mode changing or shorter than four hour are removed. Hence 74 intervals considered in our final selection (Table 2).

All intervals have quiet upstream (or input) solar wind conditions (Figure 7). Inspect of our selection the magnetic field and the plasma parameters and the calculated empirical density vary significantly stronger than in the solar wind intervals (Figure 8). The deviation of the simulated and the observed data is larger in this region as well. The scattered plots of the magnetic field, plasma flow speed and the densities agree well however these plots are relatively less accurate than the scattered plots of the solar wind (Figure 9a, 9b, 9c). The correlation of the simulated and the observed data is good for the magnetic field (Figure 10a), very good for the ion plasma moments and the calculated density (Figure 10c, 10e, 10g). The timeshift of the magnetic field is within five minutes mostly (Figure 10b) however the timeshift of the ion plasma moments is scattered (Figure 10d, 10f). The timeshift of the calculated EFW density seems to be more accurate (Figure 10h). Generally, the GUMICS–4 is less accurate in the magnetosheath. The magnetic field is quite good however the plasma parameters are not so good. The calculated empirical EFW density (n_{EFW}) fits better than the CIS HIA density (n_{CIS}).

3.3 Magnetosphere

To select intervals in the magnetosphere we looked for the CIS HIA OMNI directional ionflux. Where the band of the hot magnetosheath ion population (dis)appeared, the magnetosphere started/finished. The solar wind density slowly becomes zero, the magnetic field and the solar wind density drop and reach the zero value. We left 15–30 min after/before the magnetopause transition to appoint the interval in the magnetosphere. This way we found 132 intervals in the magnetosphere (Table 3) using Cluster SC3 measurements. The Cluster SC3 spends considerable time in the magnetosphere (Figure 11).

Here we show neither any correlation calculation nor comparison plot. In the magnetosphere the GUMICS–4 does not work well. Neither the magnetic field nor the plasma moments nor the N_{EFW} fit well. The solar wind velocity does not reach zero in the sim-

ulation. Instead the solar wind enters to the night side magnetosphere. The solar wind CIS HIA ion plasma density and the calculated density from spacecraft potential increase closer to the Earth (plasmasphere). The GUMICS–4 density is low there. We calculated the dipole field in GSE using Tsyganenko geotool box [Tsyganenko, 1995] and subtracted from both the observed and the simulated magnetic field B_z data. The correlation of these corrected magnetic field measurements and simulations is very low too.

344 3.4 Bow shock, magnetopause, neutral sheet

345 78 intervals are selected when the Cluster SC3 crossed the terrestrial bow shock
 346 once or multiple times. When the spacecraft crosses the bow shock inwards the magni-
 347 tude of the magnetic field and the solar wind density increases 4-5 times (from 5 nT or
 348 5 cm^{-3} , respectively), the solar wind speed drops from 400–600 km/s to 100–300 km/s;
 349 furthermore the narrow band on the omnidirectional Cluster CIS HIA ion spectra is widened.
 350 The Cluster measurements are 1-min averaged and the GUMICS–4 simulations has 5-
 351 min resolution hence all bow shock transitions of the virtual spacecraft are slower and
 352 smoother. Additionally, the multiple bow shock transitions are not visible in the GUMICS
 353 simulations. The code reacts slowly for such sudden changes. The magnetic signatures
 354 fit better than the calculated plasma moments. The jump of the ion plasma parameters
 355 and the derived Cluster EFW density of the simulations are shifted to the measurements.
 356 Generally, the density and the velocity of the simulations seem to be less accurate than
 357 the magnetic field of the simulations.

358 56 intervals are selected around magnetopause crossings (Anekallu, private com-
 359 munication). When the spacecraft crosses the magnetopause inward direction the mag-
 360 nitude of the magnetic field increases, the solar wind speed drops from 100–300 km/s to
 361 zero, the plasma density becomes zero; furthermore the wide band on the omnidirectional
 362 Cluster CIS HIA ion spectra disappears. These changes are not that fast. The location
 363 of the magnetopause is well determined by the Cluster SC3 measurements. However, it
 364 is very difficult to identify the magnetopause crossings in the simulation data. The 5-
 365 min resolution of the simulations provides smooth and averaged curves without sharp
 366 changes. Furthermore, the magnetopause crossings very often cannot be seen in the sim-
 367 ulations. Or when the magnetopause crossings are clearly identified in both simulations
 368 and spacecraft measurements the events are shifted. The accuracy of the model is lower
 369 for the dayside magnetopause locations.

370 Nine intervals are chosen around Cluster SC3 neutral sheet crossings (Figure 12;
 371 Table 6; Tanskanen, private communication). The neutral sheets location is determined
 372 using the results of the Boundary Layet Identification Code (BLIC) Project [Facskó *et al.*,
 373 in preparation]. The BLIC code determines the neutral sheet crossing Cluster FGM mag-
 374 netic field measurements using Wang and Xu [1994]’s method. When the solar wind speed
 375 is almost zero; furthermore the CIS HIA density and the EFW calculated density are
 376 almost zero too; finally the GSE Z component of the magnetic field changes is a sign of
 377 the code indicated neutral sheet crossing (Figure 13; red and blue curves). Surprisingly
 378 the neutral sheet crossings are visible very well in the GUMICS simulations (Figure 13;
 379 black curves). For five events (from nine Cluster SC3 crossings) the GUMICS–4 also pro-
 380 vides similar smoothed parameters and change of sign of the B_z component. This is a
 381 very good result because the tail in the GUMICS–4 simulations is significantly smaller
 382 than the observed reality [Gordeev *et al.*, 2013; Facskó *et al.*, 2016]; furthermore the so-
 383 lar wind enters the tail in MHD simulations generally [Kallio and Facskó, 2015].

384 4 Discussion

385 The agreement of the solar wind B_z , V_x and n_{EFW} with the similar GUMICS sim-
 386 ulation parameters is very good (Figure 4a, 4b, 4c, blue). The agreement of the n_{CIS}
 387 is worse (Figure 4c, red). It was expected because the n_{EFW} depends on the spacecraft
 388 potential provided by the EFW instrument. However, the CIS instrument has many modes
 389 for measuring the plasma parameters and it needs periodical calibration too. The cor-
 390 relation of the solar wind V_x , n_{CIS} and n_{EFW} with the similar GUMICS simulation pa-
 391 rameters is greater than 0.9 (Figure 5c, 5e, 5g). The correlation of the B_z is also greater
 392 than 0.8 (Figure 5a). Both numbers prove very high correlation. The inbound wall of
 393 the GUMICS–4 code is at $32 R_E$ [Janhunen *et al.*, 2012], the nose of the terrestrial bow
 394 shock is at about $20 R_E$. If the solar wind speed is 400 km/s, then this spatial distance
 395 means less than 5 minutes delay, so it should not be visible. 80% of the intervals sup-
 396 port this theory but 20 % not. In these cases the one-minute resolution B_z , n_{CIS} or the
 397 n_{EFW} parameters have a sudden jump or variation that the simulation cannot follow,
 398 or the resolution of the simulation data (5 minutes) is too small to see these variations.
 399 Therefore, the correlation calculation is not accurate in these cases. Previously the OMNI
 400 data was compared to the Cluster data and the Cluster measurements were compared
 401 to the GUMICS–4 [Facskó *et al.*, 2016]. The comparison suggests that the GUMICS–4

402 results should be similar with the OMNI data. Furthermore, we calculate correlation func-
 403 tions in the solar wind, where there is no significant perturbation of the input param-
 404 eters in the simulation box. Therefore, we get an expected result after comparing the
 405 two different correlation calculations.

406 In the magnetosheath we get worse agreement with the GUMICS simulation data
 407 (Figure 9a, 9b, 9c). However, it just means a larger uncertainty of the scattered plot.
 408 The general reason of this larger uncertainty seems to be the larger number of points.
 409 The slowed down solar wind shows strong turbulence. This phenomena explains the higher
 410 variations of the B_z magnetic field on Figure 9a. The solar wind V_x , n_{CIS} and n_{EFW}
 411 agree better than the magnetic field component (Figure 9b, 9c). Here there is no devi-
 412 ation between the densities derived in different ways (n_{CIS} and n_{EFW}) on Figure 9c.
 413 Figure 10 seems to contradict these statements above. The larger uncertainty of the B_z
 414 is visible on Figure 10a. However, that correlation is still good on Figure 10b. The other
 415 parameters have larger (> 0.9) correlation on Figure 10c, 10e, 10g. However, the time
 416 shifts on Figure 10d, 10f, 10h seem to be worse. Actually here the time shifts are worse
 417 because the shape of the time series in the magnetosheath looks very similar. Hence, the
 418 correlation calculation provides larger time shifts for the ion plasma parameters and the
 419 n_{EFW} .

420 In the magnetosphere the GUMICS–4 does not work well. The GUMICS–4 uses
 421 a tilted dipole to describe the terrestrial magnetic field [Janhunen *et al.*, 2012]. After re-
 422 moving the magnetic dipole from the magnetic field measurements of the Cluster SC3
 423 and the simulation we get very low correlations and unacceptable time shifts (not shown).
 424 In the inner magnetosphere the tilted dipole is an insufficient description. However, the
 425 plasma momentums and the n_{EFW} do not fit either. The MHD approach lost its valid-
 426 ity in the inner magnetosphere domain therefore the V_x and the n of the simulations do
 427 not agree to the V_x , the n_{CIS} and the n_{EFW} measured by the Cluster SC3. Within the
 428 $3.7 R_E$ domain another model is necessary that contains more physics as you can see it
 429 in other global MHD codes [Lyon *et al.*, 2004; Raeder *et al.*, 2008; Powell *et al.*, 1999;
 430 Tóth *et al.*, 2012]. This result explains the limited accuracy of the cross polar cap po-
 431 tential (CPCP) and geomagnetic indices of the GUMICS simulations [Juusola *et al.*, 2014].
 432 The CPCP had good agreement of GUMICS simulations and spacecraft measurements
 433 therefore this quantity could be used for capable and relevant simulation studies [Lakka
 434 *et al.*, 2018a]. Haiducek *et al.* [2017] also made a comparison study of the geomagnetic

435 indices and the CPCP. The Space Weather Modelling Framework (SWMF) was tested.
 436 When the inner magnetosphere model was switched off in the simulation only the com-
 437 parison of the simulated and observed CPCP was good. Therefore, the reason of the dis-
 438 crepancy of the geomagnetic indices in the GUMICS simulations must be the missing
 439 inner magnetosphere model.

440 The reason of the disagreement of the simulation results and the measurements could
 441 be the code or the bad input parameters. During the 1-year run the distributions of the
 442 OMNI solar wind magnetic field B_x , B_y , B_z components (Figure 14a, 14b, 14c); solar
 443 wind velocity V_x , V_y V_z components (Figure 14d, 14e, 14f) and the solar wind P dynamic
 444 pressure are calculated (Figure 14g) from January 29, 2002 to February 2, 2003 in GSE
 445 reference frame. The intervals when the GUMICS–4 simulations and the Cluster SC3
 446 measurements disagreed are collected for intervals in the solar wind (Table 4) and the
 447 magnetosheath (Table 5). The averaged shifted OMNI parameters of the poorly agree-
 448 ing intervals from the Tables 4 and 5 are saved. The distributions of the OMNI param-
 449 eters belonging to the bad simulation results are calculated for the solar wind region (Fig-
 450 ure 15, 16 and 17) and in the magnetosheath (Figure 18, 19 and 20). In the solar wind
 451 the distributions of the OMNI B_x , B_y and B_z can be compared on Figure 14a and Fig-
 452 ure 15a, 15d, 15g, 15j; Figure 14b and Figure 15b, 15e, 15h, 15k; furthermore on Fig-
 453 ure 14c and Figure 15c, 15f, 15i, 15l. When the V_x disagrees in simulations and measure-
 454 ments on Figure 15d, 15e, 15f the distributions of the OMNI B_x , B_y and B_z are simi-
 455 lar to the distributions of the OMNI B_x , B_y and B_z on Figure 14a, 14b and 14c. When
 456 the n_{CIS} disagrees in simulations and measurements on Figure 15g, 15h, 15i the distri-
 457 butions of the OMNI B_x , B_y and B_z are similar to the distributions of the OMNI B_x ,
 458 B_y and B_z on Figure 14a, 14b and 14c. When the n_{EFW} disagrees on Figure 15j, 15k, 15l
 459 the distributions of the OMNI B_x , B_y and B_z are similar to the distributions of the OMNI
 460 B_x , B_y and B_z on Figure 14a, 14b and 14c. The distributions do not agree perfectly be-
 461 cause in Table 4 the number of the poorly correlated intervals is only 6, 12 and 9 for the
 462 V_x , the n_{CIS} and n_{CIS} components, respectively. When the B_z disagrees in simulations
 463 and measurements on Figure 15a, 15b, 15c the distributions of the OMNI B_x , B_y and
 464 B_z are not similar to the distributions of the OMNI B_x , B_y and B_z on Figure 14a, 14b
 465 and 14c. The values of the OMNI B_x , B_y and B_z are not peculiar in the solar wind. The
 466 reason of these strange spikes is that there is only one poorly correlated interval for the
 467 B_z in the solar wind according to Table 4. In the solar wind the distributions of the OMNI

468 V_x , V_y and V_z can be compared on Figure 14d and Figure 16a, 16d, 16g, 16j; Figure 14e
 469 and Figure 16b, 16e, 16h, 16k; furthermore on Figure 14f and Figure 16c, 16f, 16i, 16l.
 470 When the V_x disagrees in simulations and measurements on Figure 16d, 16e, 16f the dis-
 471 tributions of the OMNI V_x , V_y and V_z are similar to the distributions of the OMNI V_x ,
 472 V_y and V_z on Figure 14d, 14e and 14f. When the n_{CIS} disagrees on Figure 16g, 16h, 16i
 473 the distributions of the OMNI V_x , V_y and V_z are similar to the distributions of the OMNI
 474 V_x , V_y and V_z on Figure 14d, 14e and 14f. When the n_{EFW} disagrees in simulations and
 475 measurements on Figure 16j, 16k, 16l the distributions of the OMNI V_x , V_y and V_z are
 476 similar to the distributions of the OMNI V_x , V_y and V_z on Figure 14d, 14e and 14f. The
 477 distributions do not agree perfectly because in Table 4 the number of the poorly corre-
 478 lated intervals is only 6, 12 and 9 for the V_x , the n_{CIS} and n_{CIS} components, respec-
 479 tively. When the B_z disagrees on Figure 16a, 16b, 16c the distributions of the OMNI V_x ,
 480 V_y and V_z are not similar to the distributions of the OMNI V_x , V_y and V_z on Figure 14d, 14e
 481 and 14f. The values of the OMNI V_x , V_y and V_z are not peculiar in the solar wind. The
 482 reason of these strange spikes is that there is only one poorly correlated interval for the
 483 B_z in the solar wind according to Table 4. In the solar wind the distributions of the OMNI
 484 P can be compared on Figure 14g and Figure 17a, 17b, 17c, 17d. When the V_x disagrees
 485 in simulations and measurements on Figure 17b the distribution of the OMNI P is sim-
 486 ilar to the distributions of the OMNI P on Figure 14g. When the n_{CIS} disagrees in sim-
 487 ulations and measurements on Figure 17c the distribution of the OMNI P is similar to
 488 the distributions of the OMNI P on Figure 14g. When the n_{EFW} disagrees in simula-
 489 tions and measurements on Figure 17d the distribution of the OMNI P is similar to the
 490 distributions of the OMNI P on Figure 14g. The distributions do not agree perfectly be-
 491 cause in Table 4 the number of the poorly correlated intervals is only 6, 12 and 9 for the
 492 V_x , the n_{CIS} and n_{CIS} components, respectively. When the B_z disagrees on Figure 17a
 493 the distribution of the OMNI P is not similar to the distribution of the OMNI P on Fig-
 494 ure 14g. The values of the OMNI P are not peculiar in the solar wind. The reason of
 495 these strange spike is that there is only one poorly correlated interval for the B_z in the
 496 solar wind according to Table 4. In the magnetosheath the distributions of the OMNI
 497 B_x , B_y and B_z can be compared on Figure 14a and Figure 18a, 18d, 18g, 18j; Figure 14b
 498 and Figure 18b, 18e, 18h, 18k; furthermore on Figure 14c and Figure 18c, 18f, 18i, 18l.
 499 When the B_z disagrees in simulations and measurements on Figure 18a, 18b, 18c the dis-
 500 tributions of the OMNI B_x , B_y and B_z are similar to the distributions of the OMNI B_x ,

501 B_y and B_z on Figure 14a, 14b and 14c. When the V_x disagrees in simulations and mea-
 502 surements on Figure 18d, 18e, 18f the distributions of the OMNI B_x , B_y and B_z are sim-
 503 ilar to the distributions of the OMNI B_x , B_y and B_z on Figure 14a, 14b and 14c. When
 504 the n_{CIS} disagrees in simulations and measurements on Figure 18g, 18h, 18i the distri-
 505 butions of the OMNI B_x , B_y and B_z are similar to the distributions of the OMNI B_x ,
 506 B_y and B_z on Figure 14a, 14b and 14c. When the n_{EFW} disagrees on Figure 18j, 18k, 18l
 507 the distributions of the OMNI B_x , B_y and B_z are similar to the distributions of the OMNI
 508 B_x , B_y and B_z on Figure 14a, 14b and 14c. The distributions agree quite well because
 509 in Table 5 the number of the poorly correlated intervals 18, 50, 33 and 30 for the B_z ,
 510 the V_x , the n_{CIS} and n_{CIS} components, respectively. The number of cases are higher
 511 and the values of the OMNI B_x , B_y and B_z are not peculiar in the magnetosheath. In
 512 the magnetosheath the distributions of the OMNI V_x , V_y and V_z can be compared on
 513 Figure 14d and Figure 19a, 19d, 19g, 19j; Figure 14e and Figure 19b, 19e, 19h, 19k; fur-
 514 thermore on Figure 14f and Figure 19c, 19f, 19i, 19l. When the B_z disagrees on Figure 19a, 19b, 19c
 515 the distributions of the OMNI V_x , V_y and V_z are similar to the distributions of the OMNI
 516 V_x , V_y and V_z on Figure 14d, 14e and 14f. When the V_x disagrees in simulations and mea-
 517 surements on Figure 19d, 19e, 19f the distributions of the OMNI V_x , V_y and V_z are sim-
 518 ilar to the distributions of the OMNI V_x , V_y and V_z on Figure 14d, 14e and 14f. When
 519 the n_{CIS} disagrees on Figure 19g, 19h, 19i the distributions of the OMNI V_x , V_y and V_z
 520 are similar to the distributions of the OMNI V_x , V_y and V_z on Figure 14d, 14e and 14f.
 521 When the n_{EFW} disagrees in simulations and measurements on Figure 19j, 19k, 19l the
 522 distributions of the OMNI V_x , V_y and V_z are similar to the distributions of the OMNI
 523 V_x , V_y and V_z on Figure 14d, 14e and 14f. The distributions agree quite well because in
 524 Table 5 the number of the poorly correlated intervals 18, 50, 33 and 30 for the B_z , the
 525 V_x , the n_{CIS} and n_{CIS} components, respectively. The number of cases are higher and
 526 the values of the OMNI V_x , V_y and V_z are not peculiar in the magnetosheath. In the mag-
 527 netosheath the distributions of the OMNI P can be compared on Figure 14g and Fig-
 528 ure 20a, 20b, 20c, 20d. When the B_z disagrees on Figure 20a the distribution of the OMNI
 529 P is similar to the distribution of the OMNI P on Figure 14g. When the V_x disagrees
 530 in simulations and measurements on Figure 20b the distribution of the OMNI P is sim-
 531 ilar to the distributions of the OMNI P on Figure 14g. When the n_{CIS} disagrees in sim-
 532 ulations and measurements on Figure 20c the distribution of the OMNI P is similar to
 533 the distributions of the OMNI P on Figure 14g. When the n_{EFW} disagrees in simula-

tions and measurements on Figure 20d the distribution of the OMNI P is similar to the distributions of the OMNI P on Figure 14g. The distributions do not agree perfectly because in Table 5 the number of the poorly correlated intervals is only 6, 12 and 9 for the V_x , the n_{CIS} and n_{CIS} components, respectively. The distributions agree quite well because in Table 5 the number of the poorly correlated intervals 18, 50, 33 and 30 for the B_z , the V_x , the n_{CIS} and n_{CIS} components, respectively. The number of cases are higher and the values of the OMNI P are not peculiar in the magnetosheath. The inaccuracy of the GUMICS-4 simulations does not depend on the OMNI parameters in the solar wind and magnetosheath regions. The same study does not need to be done for the magnetosphere because the deviance of the measurements and the simulations is so large that it cannot be caused by the wrong OMNI solar wind parameters.

The bow shock positions agree in the GUMICS simulations and the Cluster SC3 measurements. However, the magnetopause locations do not fit as good as the bow shock in simulations and observations. In simulations the location of the magnetopause is determined by currents densities or particle density gradients [García and Hughes, 2007; Gordeev et al., 2013, see references therein]. In this paper the previously saved simulation parameters along the virtual Cluster SC3 orbit are analysed. Therefore, the above mentioned methods cannot be applied. The reason of the inaccuracy of the magnetopause positions in the simulations must be the missing inner magnetosphere and ring current module. This discrepancy of the magnetopause location agrees with the results of Gordeev et al. [2013] and Facskó et al. [2016]. Gordeev et al. [2013] compared synthetic GUMICS runs with empirical formula of the magnetopause locations. Facskó et al. [2016] used OMNI solar wind data as input and got the same result as Gordeev et al. [2013] and this paper. Surprisingly the neutral sheets are visible in both simulations and observations (Figure 13, Table 6). This experience is exceptional because the night side magnetosphere of the GUMICS–4 simulations is small and twisted [Gordeev et al., 2013; Facskó et al., 2016]. However, in these cases the IMF has no large B_y component. From Facskó et al. [2016] we know that the GUMICS has normal long tail (or night side magnetosphere) if the B_y is small.

5 Summary and conclusions

Based on the previously created 1-year long GUMICS–4 run global MHD simulation results are compared with Cluster SC3 magnetic field, solar wind velocity and den-

566 sity measurements along the spacecraft orbit. Intervals are selected when the Cluster SC3
 567 and the virtual space probe are situated in the solar wind, magnetosheath and the mag-
 568 netosphere and their correlation are calculated. Bow shock, magnetopause and neutral
 569 sheet crossings are selected and their visibility and relative position are compared. We
 570 achieved the following results:

- 571 1. In the solar wind the agreement of the B_z , the V_x and the n_{EFW} is very good, fur-
 572 thermore the agreement of the n_{CIS} is also good.
- 573 2. In the magnetosheath the agreement of the magnetic field component, the ion plasma
 574 moments and the calculated empirical density is a bit worse than in the solar wind.
 575 The V_x , the n_{EFW} and the n_{CIS} fits better than the B_z component in the mag-
 576 netosheath. Their agreement is still good. The reason of the deviation is the tur-
 577 bulent behavior of the slowed down and termalised turbulent solar wind.
- 578 3. In neither the dayside nor the nightside magnetosphere can the GUMICS-4 pro-
 579 vide realistic results. The simulation outputs and the spacecraft measurement dis-
 580 agree in this region. The reason of this deviation must be the missing coupled in-
 581 ner magnetosphere model. The applied tilted dipole approach is not satisfactory
 582 in the magnetosphere at all.
- 583 4. The GUMICS-4 code causes the deviations between the simulations and the space-
 584 craft measurements because the upstream solar wind conditions seem to be nor-
 585 mal when the disagreement of the different kinds of time series is large.
- 586 5. The position of the bow shock and the neutral sheet agrees well in the simulations
 587 and the Cluster SC3 magnetic field, ion plasma moments and derived electron den-
 588 sity measurements in this study. The position of the magnetopause does not fit
 589 that well. The reason of this latest discrepancy must be the missing coupled in-
 590 ner magnetosphere model too.

591 The GUMICS-4 has incredible scientific and strategic importance for the European Space
 592 Weather and Scientific community. This code developed in the Finnish Meteorological
 593 Institute is the most developed and tested, widely used tool for modelling the cosmic en-
 594 viroment of the Earth in the old continent. Since the 1-year run was made some bugs
 595 of the code were fixed and the parallel version (the GUMICS-5) was developed (Honko-
 596 nen, private communication) however the parallel GUMICS is not been available on the
 597 CCMC or the VSWMC yet. We believe that the scientific community will have access

598 to the new version and an inner magnetosphere model will be two way coupled to the
 599 existing configuration of the simulation tool.

600 **Acknowledgments**

601 The OMNI data were obtained from the GSFC/SPDF OMNIWeb interface at <http://omniweb.gsfc.nasa.gov>.
 602 The authors thank the FGM Team (PI: Chris Carr), the CIS Team (PI: Iannis Dandouras),
 603 the WHISPER Team (PI: Jean-Louis Rauch), the EFW Team (PI: Mats Andre) and the
 604 Cluster Science Archive for providing FGM magnetic field, CIS HIA ion plasma and WHIS-
 605 PER electron density measurements. Data analysis was partly done with the QSAS sci-
 606 ence analysis system provided by the United Kingdom Cluster Science Centre (Impe-
 607 rial College London and Queen Mary, University of London) supported by the Science
 608 and Technology Facilities Council (STFC). Eija Tanskanen acknowledges financial sup-
 609 port from the Academy of Finland for the ReSoLVE Centre of Excellence (project No. 272157).
 610 Gábor Facskó thanks Anna-Mária Vígh for improving the English of the paper. The au-
 611 thors thank Pekka Janhunen for developing the GUMICS–4 code; furthermore Minna
 612 Palmroth and Zoltán Vörös for the useful discussions. The work of Gábor Facskó was
 613 supported by mission science funding for the Van Allen Probes mission, the American
 614 Geophysical Union and the HAS Research Centre for Astronomy and Earth Sciences,
 615 Sopron, Hungary. For further use of the year run data, please contact Minna Palmroth
 616 (minna.palmroth@helsinki.fi) or use the archive of the Community Coordinated Mod-
 617 elling Center (https://ccmc.gsfc.nasa.gov/publications/posted_runs/FacskoEA2016.php).
 618

619 **References**

- 620 Balogh, A., M. W. Dunlop, S. W. H. Cowley, D. J. Southwood, J. G. Thomlinson,
 621 K. H. Glassmeier, G. Musmann, H. Luhr, S. Buchert, M. H. Acuna, D. H. Fair-
 622 field, J. A. Slavin, W. Riedler, K. Schwingenschuh, and M. G. Kivelson (1997),
 623 The Cluster Magnetic Field Investigation, *Space Science Reviews*, 79, 65–91, doi:
 624 [10.1023/A:1004970907748](https://doi.org/10.1023/A:1004970907748).
- 625 Balogh, A., C. M. Carr, M. H. Acuña, M. W. Dunlop, T. J. Beek, P. Brown,
 626 K. Fornaçon, E. Georgescu, K. Glassmeier, J. Harris, G. Musmann, T. Oddy, and
 627 K. Schwingenschuh (2001), The Cluster Magnetic Field Investigation: overview of
 628 in-flight performance and initial results, *Annales Geophysicae*, 19, 1207–1217.

- 629 Bartels, J., N. H. Heck, and H. F. Johnston (1939), The three-hour-range index mea-
630 suring geomagnetic activity, *Terrestrial Magnetism and Atmospheric Electricity*
631 (*Journal of Geophysical Research*), 44, 411, doi:10.1029/TE044i004p00411.
- 632 Blagau, A., I. Dandouras, A. Barthe, S. Brunato, G. Facskó, and V. Constanti-
633 nescu (2013), In-flight calibration of Hot Ion Analyser onboard Cluster, *Geo-*
634 *scientific Instrumentation, Methods and Data Systems Discussions*, 3, 407–435,
635 doi:10.5194/gid-3-407-2013.
- 636 Blagau, A., I. Dandouras, A. Barthe, S. Brunato, G. Facskó, and V. Constantinescu
637 (2014), In-flight calibration of the Hot Ion Analyser on board Cluster, *Geoscientific*
638 *Instrumentation, Methods and Data Systems*, 3, 49–58, doi:10.5194/gi-3-49-
639 2014.
- 640 Chittenden, J. P., S. V. Lebedev, C. A. Jennings, S. N. Bland , and A. Ciardi
641 (2004), X-ray generation mechanisms in three-dimensional simulations of wire
642 array Z-pinches, *Plasma Physics and Controlled Fusion*, 46(12B), B457–B476,
643 doi:10.1088/0741-3335/46/12B/039.
- 644 Ciardi, A., S. V. Lebedev, A. Frank, E. G. Blackman, J. P. Chittenden, C. J. Jen-
645 nings, D. J. Ampleford, S. N. Bland, S. C. Bott, J. Rapley, G. N. Hall, F. A.
646 Suzuki-Vidal, A. Marocchino, T. Lery, and C. Stehle (2007), The evolution of
647 magnetic tower jets in the laboratory, *Physics of Plasmas*, 14(5), 056,501–056,501,
648 doi:10.1063/1.2436479.
- 649 Credland, J., G. Mecke, and J. Ellwood (1997), The Cluster Mission: ESA'S
650 Spacefleet to the Magnetosphere, *Space Science Reviews*, 79, 33–64, doi:
651 10.1023/A:1004914822769.
- 652 Davis, T. N., and M. Sugiura (1966), Auroral electrojet activity index AE and its
653 universal time variations, *Journal of Geophysical Research*, 71, 785–801, doi:
654 10.1029/JZ071i003p00785.
- 655 Décréau, P. M. E., P. Fergeau, V. Krasnoselskikh, E. Le Guirriec, M. Lévéque,
656 P. Martin, O. Randriamboarison, J. L. Rauch, F. X. Sené, H. C. Séran, J. G.
657 Trotignon, P. Canu, N. Cornilleau, H. de Féraudy, H. Alleyne, K. Yearby, P. B.
658 Mögensen, G. Gustafsson, M. André, D. C. Gurnett, F. Darrouzet, J. Lemaire,
659 C. C. Harvey, P. Travnicek, and Whisper Experimenters Group (2001), Early re-
660 sults from the Whisper instrument on Cluster: an overview, *Annales Geophysicae*,
661 19, 1241–1258, doi:10.5194/angeo-19-1241-2001.

- 662 Escoubet, C. P., M. Fehringer, and M. Goldstein (2001), Introduction The Cluster
663 mission, *Annales Geophysicae*, 19, 1197–1200, doi:10.5194/angeo-19-1197-2001.
- 664 Facskó, G., I. Honkonen, T. Živković, L. Palin, E. Kallio, K. Ågren, H. Opgenoorth,
665 E. I. Tanskanen, and S. Milan (2016), One year in the Earth's magnetosphere: A
666 global MHD simulation and spacecraft measurements, *Space Weather*, 14, 351–
667 367, doi:10.1002/2015SW001355.
- 668 Facskó, G., T. B. Balogh, E. I. Anekallu, C. R. and Tanskanen, P. Peitso, L. Degener,
669 M. Kangwa, T. Laitinen, and S. Laakso, H. Burley (in preparation), Bow shock
670 identification in cluster measurements, *Space Weather*.
- 671 Fazakerley, A. N., A. D. Lahiff, R. J. Wilson, I. Rozum, C. Anekallu, M. West, and
672 H. Bacai (2010a), PEACE Data in the Cluster Active Archive, *Astrophysics and
673 Space Science Proceedings*, 11, 129–144, doi:10.1007/978-90-481-3499-1_8.
- 674 Fazakerley, A. N., A. D. Lahiff, I. Rozum, D. Kataria, H. Bacai, C. Anekallu,
675 M. West, and A. Åsnes (2010b), Cluster-PEACE In-flight Calibration Status,
676 *Astrophysics and Space Science Proceedings*, 11, 281–299, doi:10.1007/978-90-481-
677 3499-1_19.
- 678 García, K. S., and W. J. Hughes (2007), Finding the Lyon-Fedder-Mobarry mag-
679 netopause: A statistical perspective, *Journal of Geophysical Research (Space
680 Physics)*, 112(A6), A06229, doi:10.1029/2006JA012039.
- 681 Gordeev, E., G. Facskó, V. Sergeev, I. Honkonen, M. Palmroth, P. Janhunen, and
682 S. Milan (2013), Verification of the GUMICS-4 global MHD code using empirical
683 relationships, *Journal of Geophysical Research (Space Physics)*, 118, 3138–3146,
684 doi:10.1002/jgra.50359.
- 685 Greenwald, R. A., K. B. Baker, J. R. Dudeney, M. Pinnock, T. B. Jones, E. C.
686 Thomas, J.-P. Villain, J.-C. Cerisier, C. Senior, C. Hanuise, R. D. Hunsucker,
687 G. Sofko, J. Koehler, E. Nielsen, R. Pellinen, A. D. M. Walker, N. Sato,
688 and H. Yamagishi (1995), Darn/Superdarn: A Global View of the Dynam-
689 ics of High-Latitude Convection, *Space Science Reviews*, 71, 761–796, doi:
690 10.1007/BF00751350.
- 691 Guild, T. B., H. E. Spence, E. L. Kepko, V. Merkin, J. G. Lyon, M. Wiltberger, and
692 C. C. Goodrich (2008a), Geotail and LFM comparisons of plasma sheet clima-
693 tology: 1. Average values, *Journal of Geophysical Research (Space Physics)*, 113,
694 A04216, doi:10.1029/2007JA012611.

- 695 Guild, T. B., H. E. Spence, E. L. Kepko, V. Merkin, J. G. Lyon, M. Wiltberger, and
696 C. C. Goodrich (2008b), Geotail and LFM comparisons of plasma sheet climatol-
697 ogy: 2. Flow variability, *Journal of Geophysical Research (Space Physics)*, 113,
698 A04217, doi:10.1029/2007JA012613.
- 699 Gustafsson, G., R. Bostrom, B. Holback, G. Holmgren, A. Lundgren, K. Stasiewicz,
700 L. Ahlen, F. S. Mozer, D. Pankow, P. Harvey, P. Berg, R. Ulrich, A. Pedersen,
701 R. Schmidt, A. Butler, A. W. C. Fransen, D. Klinge, M. Thomsen, C.-G. Faltham-
702 mar, P.-A. Lindqvist, S. Christenson, J. Holtet, B. Lybekk, T. A. Sten, P. Tan-
703 skanen, K. Lappalainen, and J. Wygant (1997), The Electric Field and Wave
704 Experiment for the Cluster Mission, *Space Science Reviews*, 79, 137–156, doi:
705 10.1023/A:1004975108657.
- 706 Gustafsson, G., M. André, T. Carozzi, A. I. Eriksson, C.-G. Fälthammar, R. Grard,
707 G. Holmgren, J. A. Holtet, N. Ivchenko, T. Karlsson, Y. Khotyaintsev, S. Klimov,
708 H. Laakso, P.-A. Lindqvist, B. Lybekk, G. Marklund, F. Mozer, K. Mursula,
709 A. Pedersen, B. Popielawska, S. Savin, K. Stasiewicz, P. Tanskanen, A. Vaivads,
710 and J.-E. Wahlund (2001), First results of electric field and density observations
711 by Cluster EFW based on initial months of operation, *Annales Geophysicae*, 19,
712 1219–1240, doi:10.5194/angeo-19-1219-2001.
- 713 Haiducek, J. D., D. T. Welling, N. Y. Ganushkina, S. K. Morley, and D. S. Oz-
714 turk (2017), SWMF Global Magnetosphere Simulations of January 2005: Geo-
715 magnetic Indices and Cross-Polar Cap Potential, *Space Weather*, 15, 1567–1587,
716 doi:10.1002/2017SW001695.
- 717 Iyemori, T. (1990), Storm-time magnetospheric currents inferred from mid-latitude
718 geomagnetic field variations, *Journal of Geomagnetism and Geoelectricity*, 42,
719 1249–1265, doi:10.5636/jgg.42.1249.
- 720 Janhunen, P., M. Palmroth, T. Laitinen, I. Honkonen, L. Juusola, G. Facskó, and
721 T. I. Pulkkinen (2012), The GUMICS-4 global MHD magnetosphere-ionosphere
722 coupling simulation, *Journal of Atmospheric and Solar-Terrestrial Physics*, 80,
723 48–59, doi:10.1016/j.jastp.2012.03.006.
- 724 Johnstone, A. D., C. Alsop, S. Burge, P. J. Carter, A. J. Coates, A. J. Coker, A. N.
725 Fazakerley, M. Grande, R. A. Gowen, C. Gurgiolo, B. K. Hancock, B. Narheim,
726 A. Preece, P. H. Sheather, J. D. Winningham, and R. D. Woodliffe (1997), Peace:
727 a Plasma Electron and Current Experiment, *Space Science Reviews*, 79, 351–398,

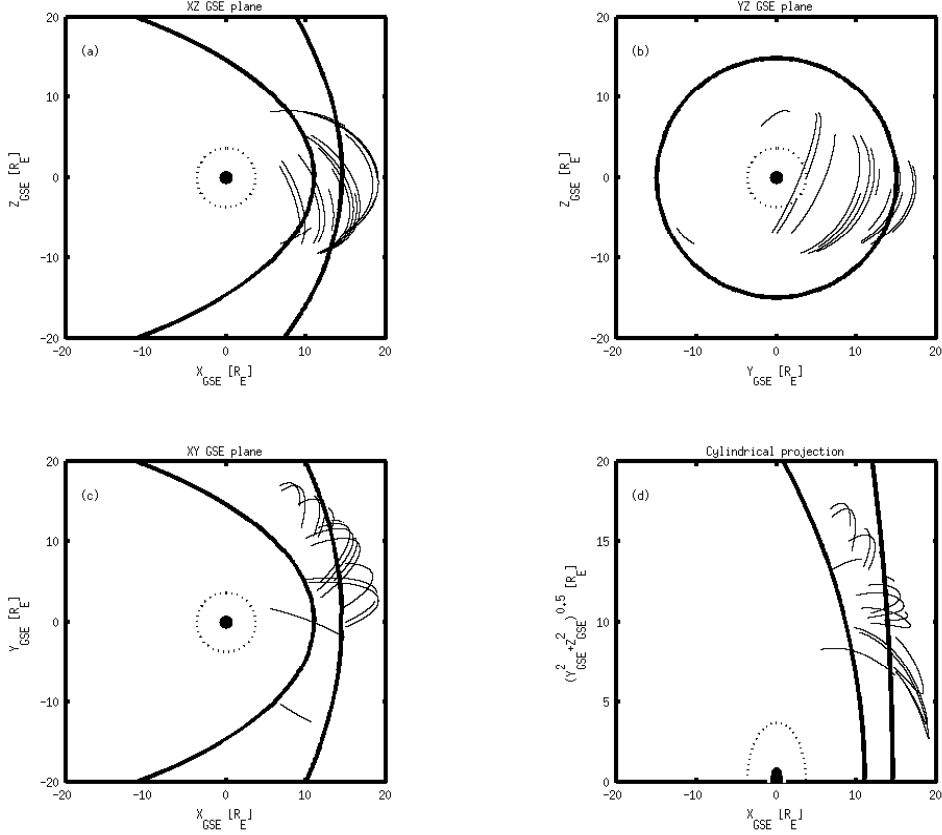
- 728 doi:10.1023/A:1004938001388.
- 729 Juusola, L., O. Amm, K. Kauristie, and A. Viljanen (2007), A model for estimating
730 the relation between the Hall to Pedersen conductance ratio and ground magnetic
731 data derived from CHAMP satellite statistics, *Annales Geophysicae*, 25, 721–736,
732 doi:10.5194/angeo-25-721-2007.
- 733 Juusola, L., G. Facskó, I. Honkonen, P. Janhunen, H. Vanhamäki, K. Kauristie,
734 T. V. Laitinen, S. E. Milan, M. Palmroth, E. I. Tanskanen, and A. Viljanen
735 (2014), Statistical comparison of seasonal variations in the GUMICS-4 global
736 MHD model ionosphere and measurements, *Space Weather*, 12, 582–600, doi:
737 10.1002/2014SW001082.
- 738 Kallio, E., and G. Facskó (2015), Properties of plasma near the moon in the magne-
739 total, *Planetary and Space Science*, 115, 69–76, doi:10.1016/j.pss.2014.11.007.
- 740 Kokubun, S., T. Yamamoto, M. H. Acuña, K. Hayashi, K. Shiokawa, and H. Kawano
741 (1994), The GEOTAIL Magnetic Field Experiment., *Journal of Geomagnetism*
742 and *Geoelectricity*, 46, 7–21, doi:10.5636/jgg.46.7.
- 743 Lakka, A., T. I. Pulkkinen, A. P. Dimmock, M. Myllys, I. Honkonen, and M. Palm-
744 roth (2018a), The Cross-Polar Cap Saturation in GUMICS-4 During High Solar
745 Wind Driving, *Journal of Geophysical Research (Space Physics)*, 123, 3320–3332,
746 doi:10.1002/2017JA025054.
- 747 Lakka, A., T. I. Pulkkinen, A. P. Dimmock, E. Kilpua, M. Ala-Lahti, I. Honko-
748 nen, M. Palmroth, and Raukunen (2018b), Icme impact at earth with low and
749 typical mach number plasma characteristics, *Annales Geophysicae Discussions*,
750 <https://doi.org/10.5194/angeo-2018-81>.
- 751 Lani, A., A. Sanna, N. Villedieu, and M. Panesi (2012), COOLFluiD an Open Com-
752 putational Platform for Aerothermodynamics and Flow-Radiation Coupling, in
753 *ESA Special Publication, ESA Special Publication*, vol. 714, p. 45.
- 754 Lyon, J. G., J. A. Fedder, and C. M. Mobarry (2004), The Lyon-Fedder-Mobarry
755 (LFM) global MHD magnetospheric simulation code, *Journal of Atmospheric and*
756 *Solar-Terrestrial Physics*, 66, 1333–1350, doi:10.1016/j.jastp.2004.03.020.
- 757 Mejnertsen, L., J. P. Eastwood, J. P. Chittenden, and A. Masters (2016), Global
758 MHD simulations of Neptune’s magnetosphere, *Journal of Geophysical Research*
759 (*Space Physics*), 121(8), 7497–7513, doi:10.1002/2015JA022272.
- 760 Mejnertsen, L., J. P. Eastwood, H. Hietala, S. J. Schwartz, and J. P. Chittenden

- 761 (2018), Global MHD Simulations of the Earth's Bow Shock Shape and Motion
762 Under Variable Solar Wind Conditions, *Journal of Geophysical Research (Space*
763 *Physics)*, 123(1), 259–271, doi:10.1002/2017JA024690.
- 764 Mukai, T., S. Machida, Y. Saito, M. Hirahara, T. Terasawa, N. Kaya, T. Obara,
765 M. Ejiri, and A. Nishida (1994), The Low Energy Particle (LEP) Experiment on-
766 board the GEOTAIL Satellite., *Journal of Geomagnetism and Geoelectricity*, 46,
767 669–692, doi:10.5636/jgg.46.669.
- 768 Peredo, M., J. A. Slavin, E. Mazur, and S. A. Curtis (1995), Three-dimensional po-
769 sition and shape of the bow shock and their variation with Alfvénic, sonic and
770 magnetosonic Mach numbers and interplanetary magnetic field orientation, *Jour-*
771 *nal of Geophysical Research*, 100, 7907–7916, doi:10.1029/94JA02545.
- 772 Poedts, S., A. Kochanov, A. Lani, C. Scolini, C. Verbeke, S. Hosteaux, E. Chané,
773 H. Deconinck, N. Mihalache, F. Diet, D. Heynderickx, J. De Keyser, E. De
774 Donder, N. B. Crosby, M. Echim, L. Rodriguez, R. Vansintjan, F. Verstringe,
775 B. Mampaey, R. Horne, S. Glauert, P. Jiggens, R. Keil, A. Glover, G. Deprez, and
776 J.-P. Luntama (2020), The Virtual Space Weather Modelling Centre, *Journal of*
777 *Space Weather and Space Climate*, 10, 14, doi:10.1051/swsc/2020012.
- 778 Powell, K. G., P. L. Roe, T. J. Linde, T. I. Gombosi, and D. L. De Zeeuw (1999), A
779 Solution-Adaptive Upwind Scheme for Ideal Magnetohydrodynamics, *Journal of*
780 *Computational Physics*, 154, 284–309, doi:10.1006/jcph.1999.6299.
- 781 Raeder, J., D. Larson, W. Li, E. L. Kepko, and T. Fuller-Rowell (2008), OpenG-
782 GCM Simulations for the THEMIS Mission, *Space Science Reviews*, 141, 535–555,
783 doi:10.1007/s11214-008-9421-5.
- 784 Reigber, C., H. Lühr, and P. Schwintzer (2002), CHAMP mission status, *Advances*
785 *in Space Research*, 30, 129–134, doi:10.1016/S0273-1177(02)00276-4.
- 786 Reme, H., J. M. Bosqued, J. A. Sauvaud, A. Cros, J. Dandouras, C. Aoustin,
787 J. Bouyssou, T. Camus, J. Cuvilo, C. Martz, J. L. Medale, H. Perrier, D. Rome-
788 fort, J. Rouzaud, C. D'Uston, E. Mobius, K. Crocker, M. Granoff, L. M. Kistler,
789 M. Popecki, D. Hovestadt, B. Klecker, G. Paschmann, M. Scholer, C. W. Carl-
790 son, D. W. Curtis, R. P. Lin, J. P. McFadden, V. Formisano, E. Amata, M. B.
791 Bavassano-Cattaneo, P. Baldetti, G. Bellucci, R. Bruno, G. Chionchio, A. di Lel-
792 lis, E. G. Shelley, A. G. Ghielmetti, W. Lennartsson, A. Korth, H. Rosenbauer,
793 R. Lundin, S. Olsen, G. K. Parks, M. McCarthy, and H. Balsiger (1997), The

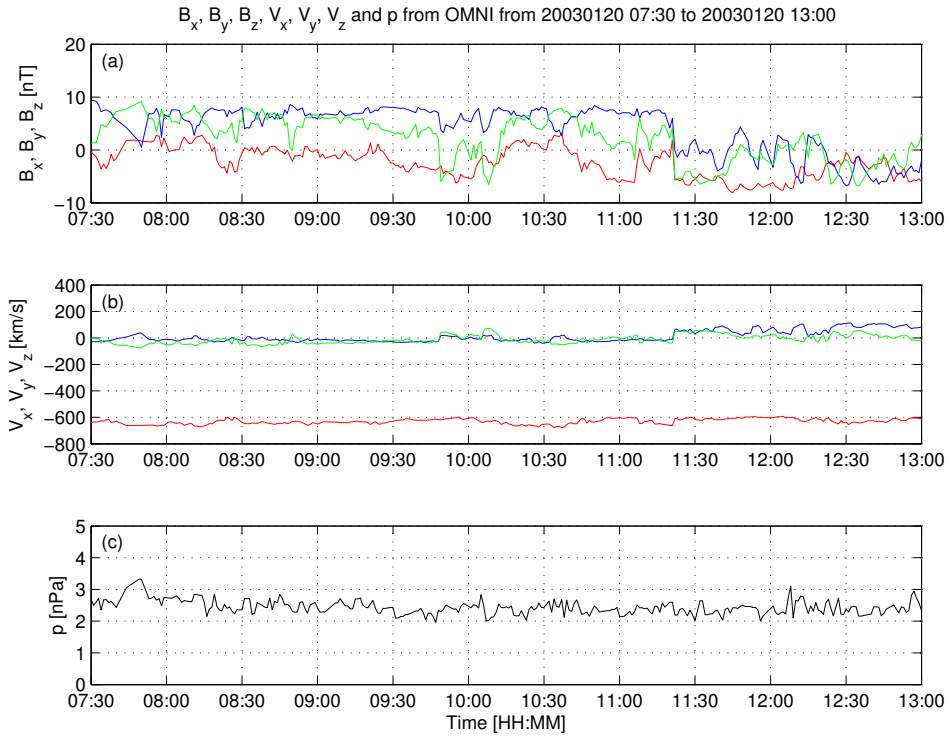
- 794 Cluster Ion Spectrometry (CIS) Experiment, *Space Science Reviews*, 79, 303–350,
795 doi:10.1023/A:1004929816409.
- 796 Rème, H., C. Aoustin, J. M. Bosqued, I. Dandouras, B. Lavraud, J. A. Sauvaud,
797 A. Barthe, J. Bouyssou, T. Camus, O. Coeur-Joly, A. Cros, J. Cuvilo, F. Ducay,
798 Y. Garbarowitz, J. L. Medale, E. Penou, H. Perrier, D. Romefort, J. Rouzaud,
799 C. Vallat, D. Alcaydé, C. Jacquey, C. Mazelle, C. D'Uston, E. Möbius, L. M.
800 Kistler, K. Crocker, M. Granoff, C. Mouikis, M. Popecki, M. Vosbury, B. Klecker,
801 D. Hovestadt, H. Kucharek, E. Kuenneth, G. Paschmann, M. Scholer, N. Sckopke,
802 E. Seidenschwang, C. W. Carlson, D. W. Curtis, C. Ingraham, R. P. Lin, J. P.
803 McFadden, G. K. Parks, T. Phan, V. Formisano, E. Amata, M. B. Bavassano-
804 Cattaneo, P. Baldetti, R. Bruno, G. Chionchio, A. di Lellis, M. F. Marcucci,
805 G. Pallocchia, A. Korth, P. W. Daly, B. Graeve, H. Rosenbauer, V. Vasyliunas,
806 M. McCarthy, M. Wilber, L. Eliasson, R. Lundin, S. Olsen, E. G. Shelley, S. Fuse-
807 lier, A. G. Ghielmetti, W. Lennartsson, C. P. Escoubet, H. Balsiger, R. Friedel, J.-
808 B. Cao, R. A. Kovrashkin, I. Papamastorakis, R. Pellat, J. Scudder, and B. Son-
809 nerup (2001), First multispacecraft ion measurements in and near the Earth's
810 magnetosphere with the identical Cluster ion spectrometry (CIS) experiment,
811 *Annales Geophysicae*, 19, 1303–1354, doi:10.5194/angeo-19-1303-2001.
- 812 Ritter, P., H. Lühr, A. Viljanen, O. Amm, A. Pulkkinen, and I. Sillanpää (2004),
813 Ionospheric currents estimated simultaneously from CHAMP satellite and IMAGE
814 ground-based magnetic field measurements: a statistical study at auroral latitudes,
815 *Annales Geophysicae*, 22, 417–430, doi:10.5194/angeo-22-417-2004.
- 816 Rostoker, G. (1972), Geomagnetic indices., *Reviews of Geophysics and Space
817 Physics*, 10, 935–950, doi:10.1029/RG010i004p00935.
- 818 Sofko, G. J., R. Greenwald, and W. Bristow (1995), Direct determination of large-
819 scale magnetospheric field-aligned currents with SuperDARN, *Geophysical Re-
820 search Letters*, 22, 2041–2044, doi:10.1029/95GL01317.
- 821 Thomsen, M. F. (2004), Why K_p is such a good measure of magnetospheric convec-
822 tion, *Space Weather*, 2, S11004, doi:10.1029/2004SW000089.
- 823 Tóth, G., I. V. Sokolov, T. I. Gombosi, D. R. Chesney, C. R. Clauer, D. L. de
824 Zeeuw, K. C. Hansen, K. J. Kane, W. B. Manchester, R. C. Oehmke, K. G. Pow-
825 ell, A. J. Ridley, I. I. Roussev, Q. F. Stout, O. Volberg, R. A. Wolf, S. Sazykin,
826 A. Chan, B. Yu, and J. Kóta (2005), Space Weather Modeling Framework: A

- 827 new tool for the space science community, *Journal of Geophysical Research (Space*
828 *Physics)*, 110, A12226, doi:10.1029/2005JA011126.
- 829 Tóth, G., B. van der Holst, I. V. Sokolov, D. L. De Zeeuw, T. I. Gombosi, F. Fang,
830 W. B. Manchester, X. Meng, D. Najib, K. G. Powell, Q. F. Stout, A. Glo-
831 cer, Y.-J. Ma, and M. Opher (2012), Adaptive numerical algorithms in space
832 weather modeling, *Journal of Computational Physics*, 231, 870–903, doi:
833 10.1016/j.jcp.2011.02.006.
- 834 Trotignon, J. G., P. M. E. Décréau, J. L. Rauch, X. Vallières, A. Rochel,
835 S. Kougblénou, G. Lointier, G. Facskó, P. Canu, F. Darrouzet, and A. Masson
836 (2010), The WHISPER Relaxation Sounder and the CLUSTER Active Archive,
837 *Astrophysics and Space Science Proceedings*, 11, 185–208, doi:10.1007/978-90-481-
838 3499-1_12.
- 839 Trotignon, J.-G., Vallières, and the WHISPER team (2011), Calibration report of
840 the whisper measurements in the cluster active archive (caa), *Tech. rep.*, LPC2E
841 CNRS, caa-est-cr-whi.
- 842 Tsyganenko, N. A. (1995), Modeling the Earth's magnetospheric magnetic field
843 confined within a realistic magnetopause, *Journal of Geophysical Research*, 100,
844 5599–5612, doi:10.1029/94JA03193.
- 845 Vörös, Z., G. Facskó, M. Khodachenko, I. Honkonen, P. Janhunen, and M. Palmroth
846 (2014), Windsock memory COnditioned RAM (CO-RAM) pressure effect: Forced
847 reconnection in the Earth's magnetotail, *Journal of Geophysical Research (Space*
848 *Physics)*, 119, 6273–6293, doi:10.1002/2014JA019857.
- 849 Wang, Z.-D., and R. L. Xu (1994), Signatures of the magnetotail neutral sheet,
850 *Geophysical Research Letters*, 21(19), 2087–2090, doi:10.1029/94GL01960.
- 851 Weimer, D. R. (2005), Improved ionospheric electrodynamic models and applica-
852 tion to calculating Joule heating rates, *Journal of Geophysical Research (Space*
853 *Physics)*, 110, A05306, doi:10.1029/2004JA010884.
- 854 Wiltberger, M., E. J. Rigler, V. Merkin, and J. G. Lyon (2017), Structure of High
855 Latitude Currents in Magnetosphere-Ionosphere Models, *Space Science Reviews*,
856 206, 575–598, doi:10.1007/s11214-016-0271-2.
- 857 Zhang, B., W. Lotko, M. J. Wiltberger, O. J. Brambles, and P. A. Damiano (2011),
858 A statistical study of magnetosphere-ionosphere coupling in the Lyon-Fedder-
859 Mobarry global MHD model, *Journal of Atmospheric and Solar-Terrestrial*

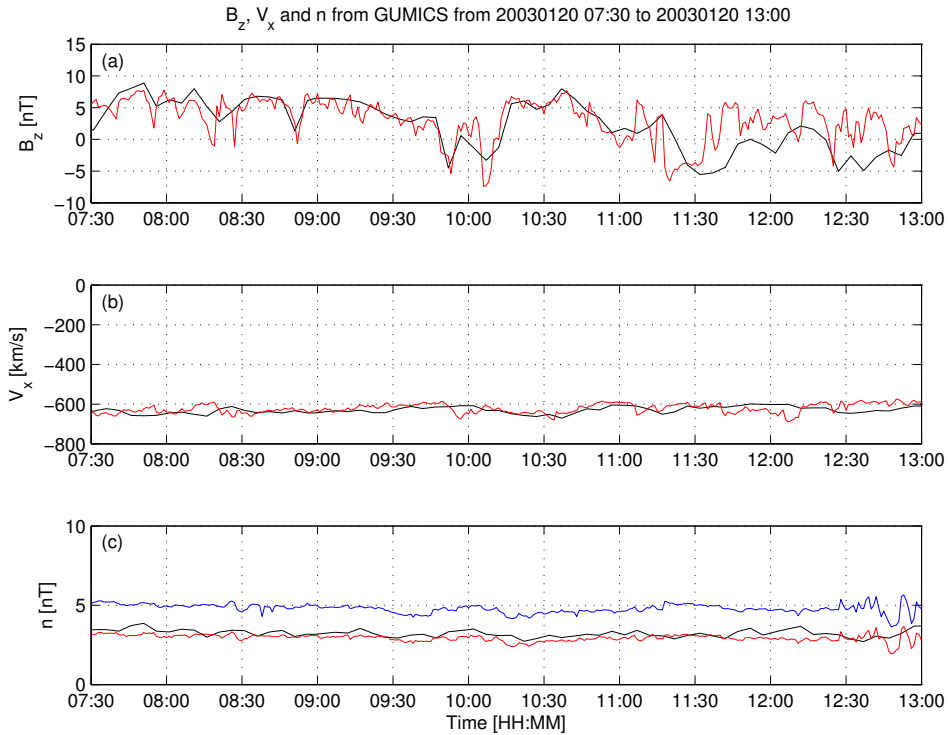
860 *Physics*, 73, 686–702, doi:10.1016/j.jastp.2010.09.027.



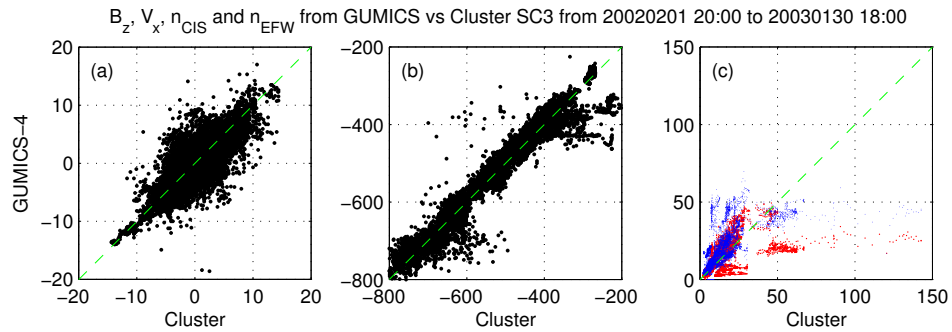
861 **Figure 1.** Cluster SC3 orbit in the solar wind in GSE system for all intervals (see Table 1).
862 (a) XZ (b) YZ (c) XY (d) Cylindrical projection. Average bow-shock and magnetopause posi-
863 tions are drawn on all plots using solid line [Perego *et al.*, 1995; Tsyganenko, 1995, respectively].
864 The black dots at $3.7 R_E$ show the boundary of the GUMICS-4 inner magnetospheric domain.
865 The black circle in the origo of all plots shows the size of the Earth.



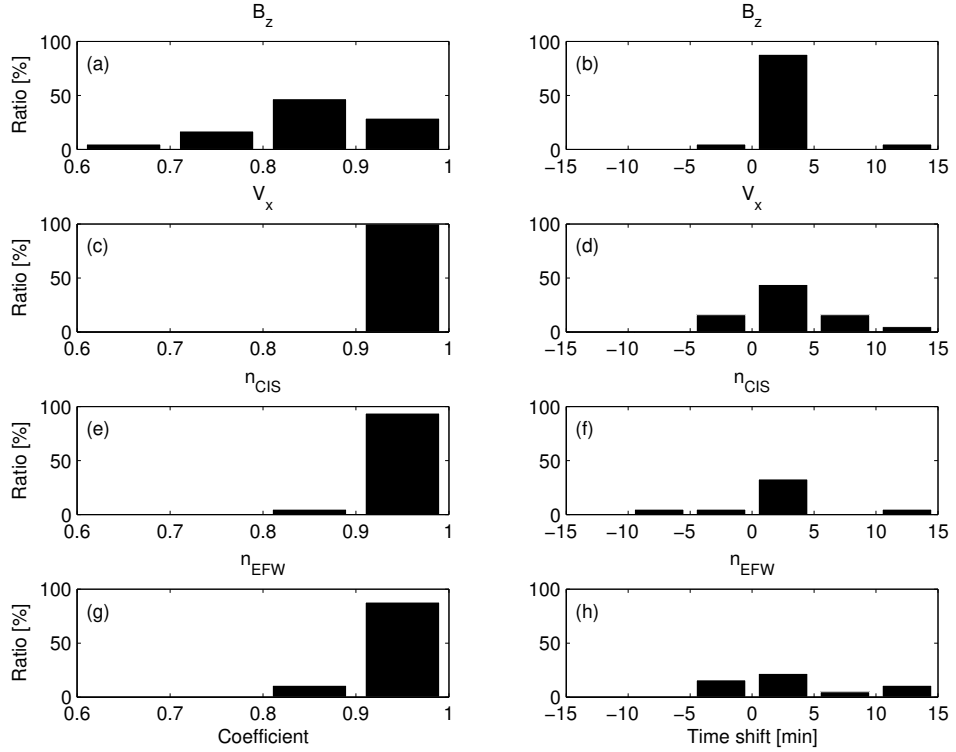
866 **Figure 2.** OMNI solar wind data in GSE system from 7:30 to 13:00 (UT) on January 20,
 867 2003. (a) Magnetic field B_x (red), B_y (green) and B_z (blue) components. (b) Solar wind velocity
 868 V_x (red), V_y (green) and V_z (blue) components. (c) The P pressure of the solar wind (black).



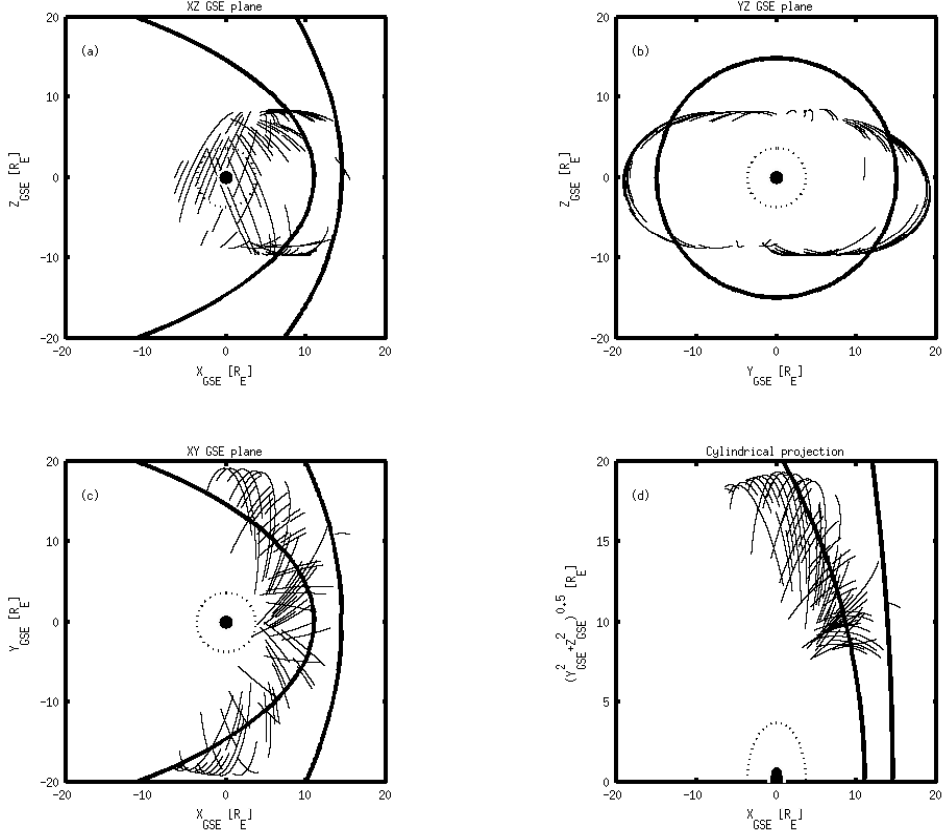
869 **Figure 3.** GUMICS-4 simulation results (black) and Cluster SC3 magnetic field Z component,
 870 ion plasma moments (red) and electron density calculated from spacecraft potential (blue) from
 871 January 20, 2003 from 7:30 to 13:00 (UT) in the solar wind in GSE system. (a) Magnetic field Z
 872 component. (b) Solar wind velocity X component (c) Solar wind density.



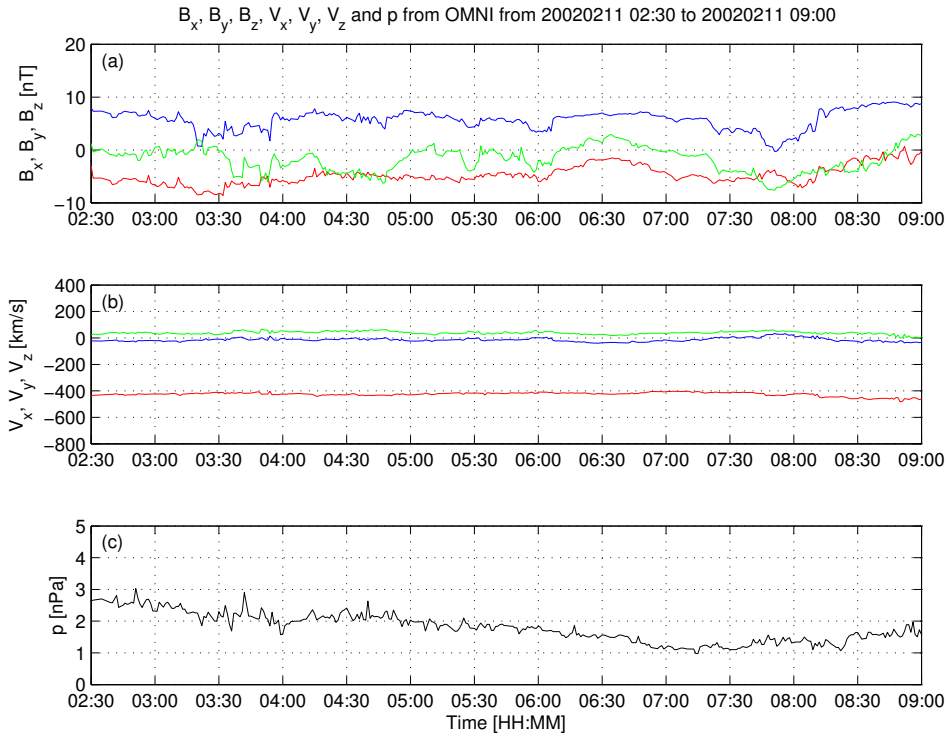
873 **Figure 4.** Scattered plots of the Cluster SC3 and GUMICS-4 simulations for all intervals in
 874 the solar wind. The dashed line is the $y=x$ line. (a) Magnetic field Z component in GSE system.
 875 (b) Solar wind velocity X component in GSE system. (c) Solar wind density measured by the
 876 CIS HIA instrument (red) and calculated from the spacecraft potential (blue).



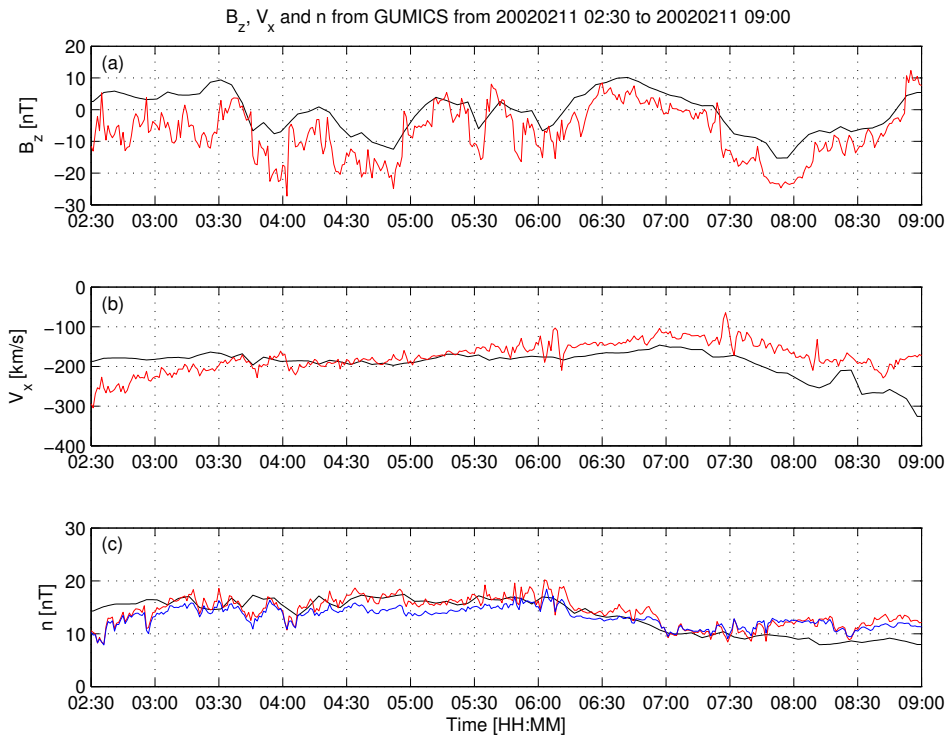
877 **Figure 5.** The distributions of the correlation coefficients (a, c, e, g) of the magnetic field Z
 878 component (B_z) in GSE system, solar wind velocity X component (V_X) in GSE system, the solar
 879 wind density measured by the CIS HIA (n_{CIS}) instrument and calculated from the spacecraft
 880 potential (n_{EFW}), respectively, for all intervals in the solar wind. The distributions of the time
 881 shifts (b, d, f, h) of the B_z , the V_X , the n_{CIS} and the n_{EFW} , respectively, for all intervals in the
 882 solar wind.



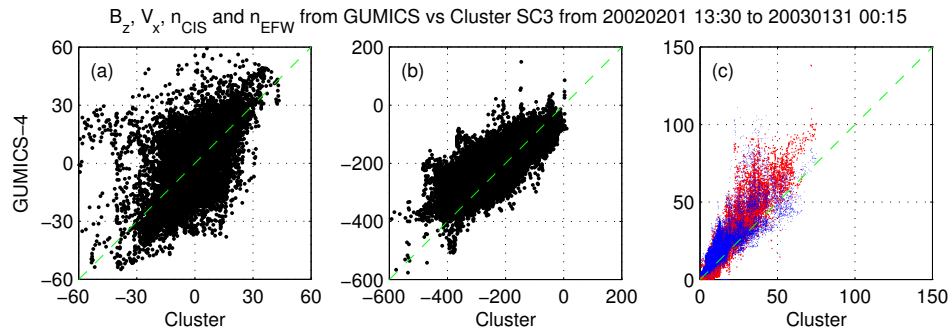
883 **Figure 6.** Cluster SC3 orbit in the magnetosheath in GSE system for all intervals (see Ta-
 884 ble 2). (a) XZ (b) YZ (c) XY (d) Cylindrical projection. Average bow-shock and magnetopause
 885 positions are drawn on all plots using solid line [Peredo *et al.*, 1995; Tsyganenko, 1995, respec-
 886 tively]. The black dots at $3.7 R_E$ show the boundary of the GUMICS-4 inner magnetospheric
 887 domain. The black circle in the origo of all plots shows the size of the Earth.



888 **Figure 7.** OMNI solar wind data in GSE system from 2:30 to 09:00 (UT) on February 11,
889 2002. (a) Magnetic field B_x (red), B_y (green) and B_z (blue) components. (b) Solar wind velocity
890 V_x (red), V_y (green) and V_z (blue) components. (c) The P pressure of the solar wind (black).



891 **Figure 8.** GUMICS-4 simulation results (black) and Cluster SC3 magnetic field Z component,
 892 ion plasma moments (red) and electron density calculated from spacecraft potential (blue) from
 893 February 11, 2002 from 2:30 to 9:00 (UT) in the magnetosheath in GSE system (a) Magnetic
 894 field Z component. (b) Solar wind velocity X component (c) Solar wind density.



895 **Figure 9.** Scattered plots of the Cluster SC3 and GUMICS-4 simulations for all intervals in
 896 the magnetosheath in GSE system. The dashed line is the $y=x$ line. (a) Magnetic field Z com-
 897 ponent. (b) Solar wind velocity X component. (c) Solar wind density measured by the CIS HIA
 898 instrument (red) and calculated from the spacecraft potential (blue).

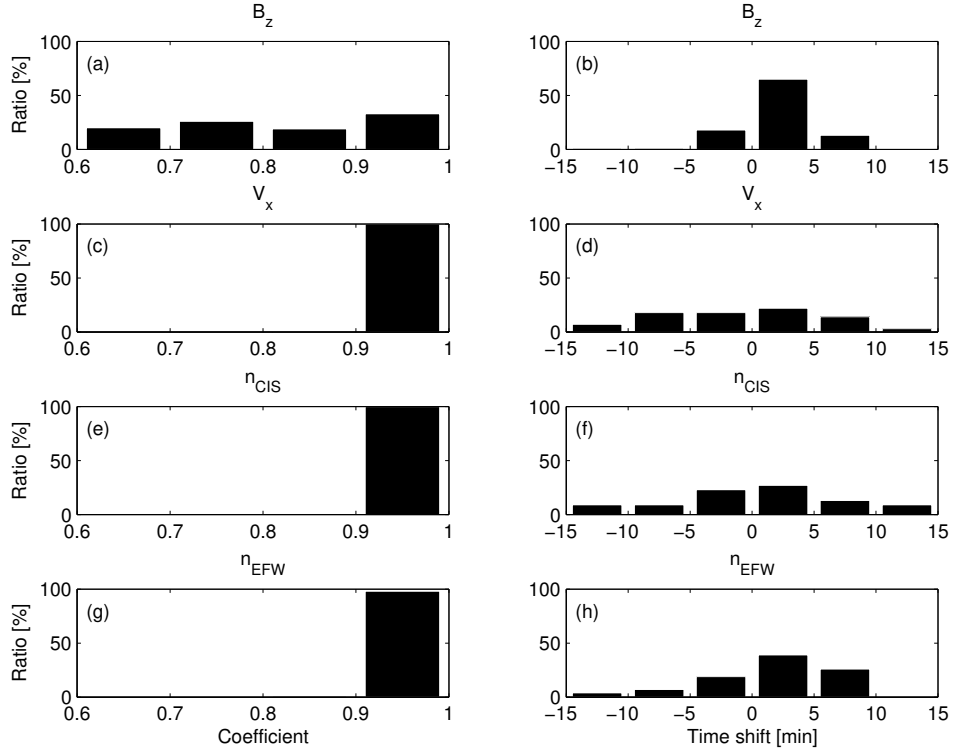
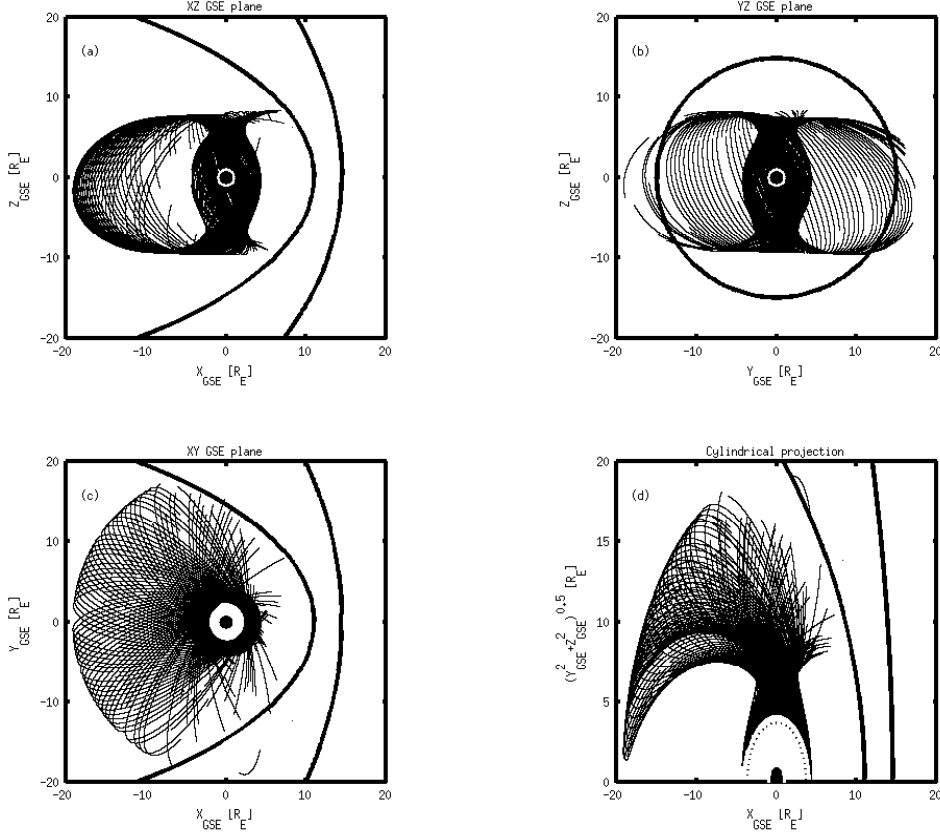
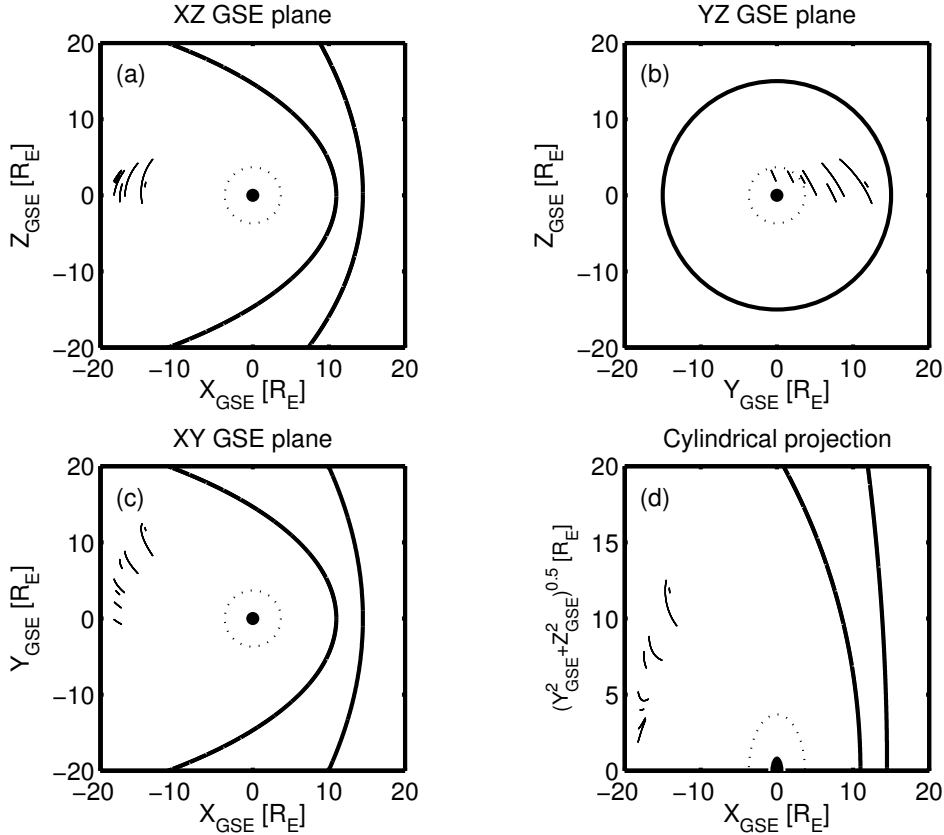


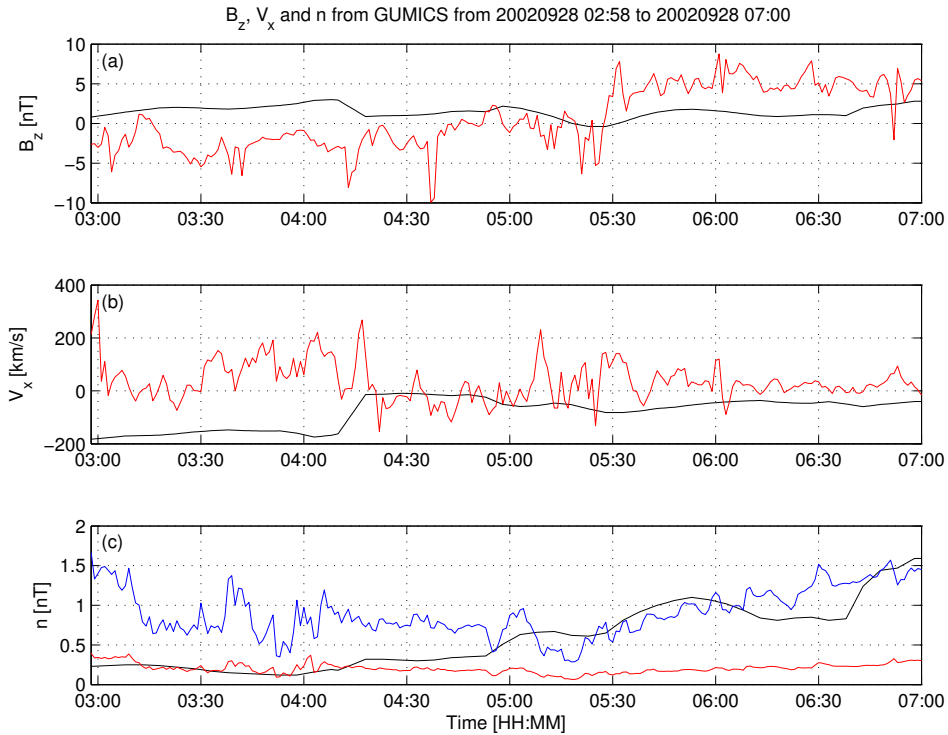
Figure 10. The distributions of the correlation coefficients (a, c, e, g) of the magnetic field Z component (B_z) in GSE system, solar wind velocity X component (V_X) in GSE system, the solar wind density measured by the CIS HIA (n_{CIS}) instrument and calculated from the spacecraft potential (n_{EFW}), respectively, for all intervals in the magnetosheath. The distributions of the time shifts (b, d, f, h) of the B_z , the V_X , the n_{CIS} and the n_{EFW}), respectively, for all intervals in the magnetosheath.



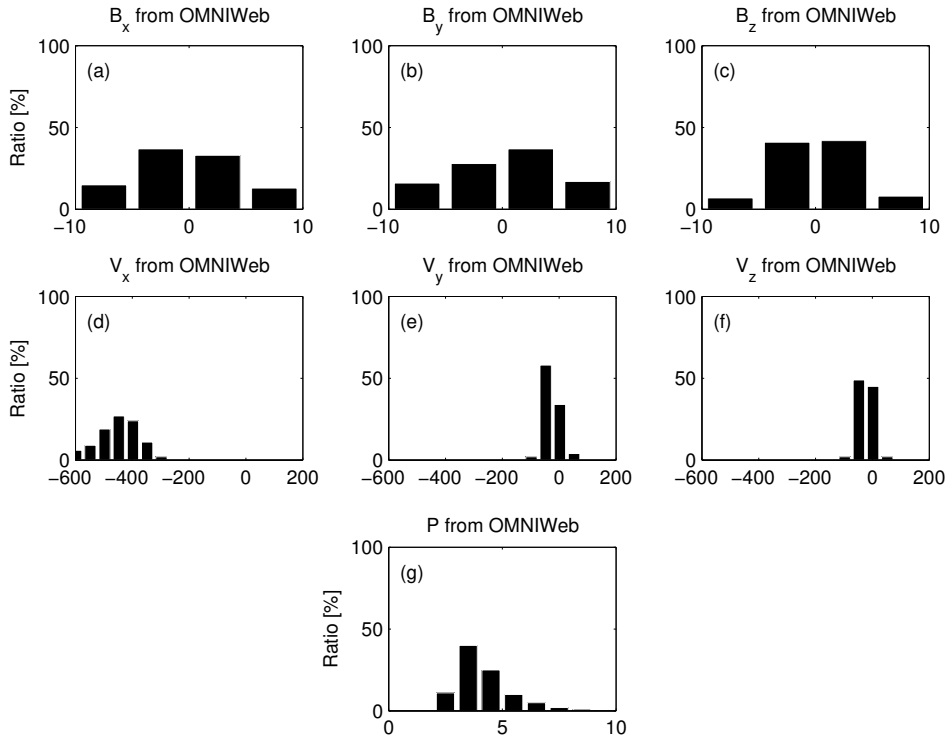
905 **Figure 11.** Cluster SC3 orbit in the magnetosphere in GSE system for all intervals (see Ta-
 906 ble 3). (a) XZ (b) YZ (c) XY (d) Cylindrical projection. Average bow-shock and magnetopause
 907 positions are drawn on all plots using solid line [Peredo *et al.*, 1995; Tsyganenko, 1995, respec-
 908 tively]. The black dots at $3.7 R_E$ show the boundary of the GUMICS-4 inner magnetospheric
 909 domain. The black circle in the origo of all plots shows the size of the Earth.



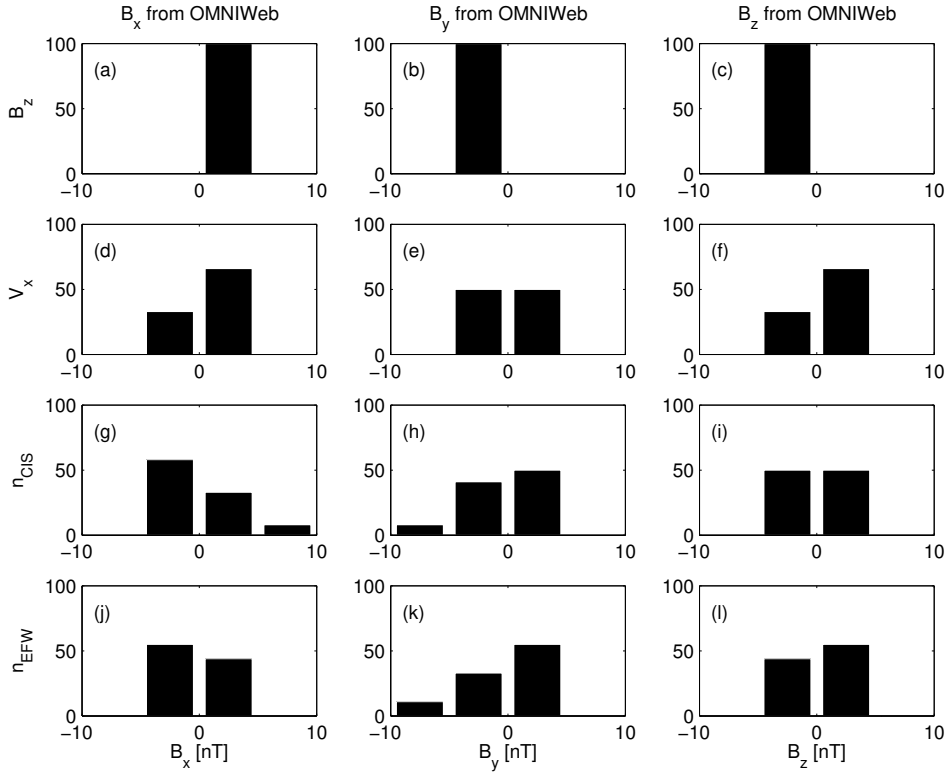
910 **Figure 12.** Cluster SC3 orbit in the tail in GSE system for all intervals (see Table 6). (a)
 911 (b) (c) (d) Cylindrical projection. Average bow-shock and magnetopause positions
 912 are drawn on all plots using solid line [Perego *et al.*, 1995; Tsyganenko, 1995, respectively]. The
 913 black dots at $3.7 R_E$ show the boundary of the GUMICS–4 inner magnetospheric domain. The
 914 black circle in the origo of all plots shows the size of the Earth.



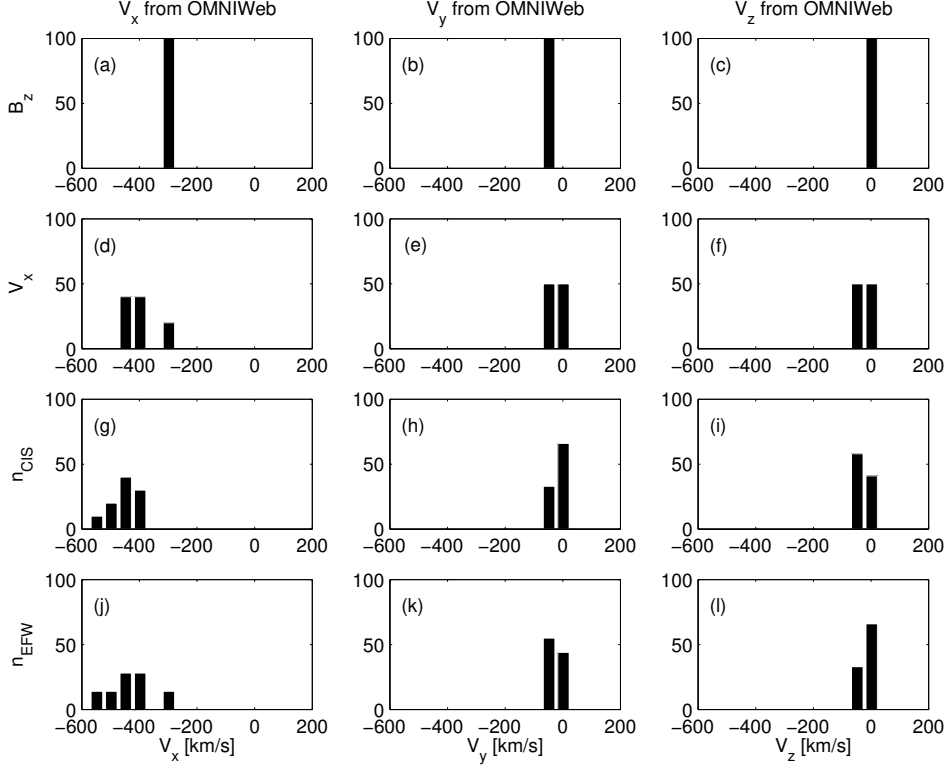
915 **Figure 13.** GUMICS-4 simulation results (black) and Cluster SC3 magnetic field Z compo-
 916 nent, ion plasma moments (red) and electron density calculated from spacecraft potential (blue)
 917 from September 28, 2002 from 2:58 to 7:00 (UT) in the tail in GSE system. (a) Magnetic field
 918 Z component. (b) Solar wind velocity X component (c) Solar wind density. From 05:15 to 05:30
 919 both the Cluster SC3 and the virtual spaceprobe of the GUMICS-4 simulation cross the neutral
 920 sheet multiple times.



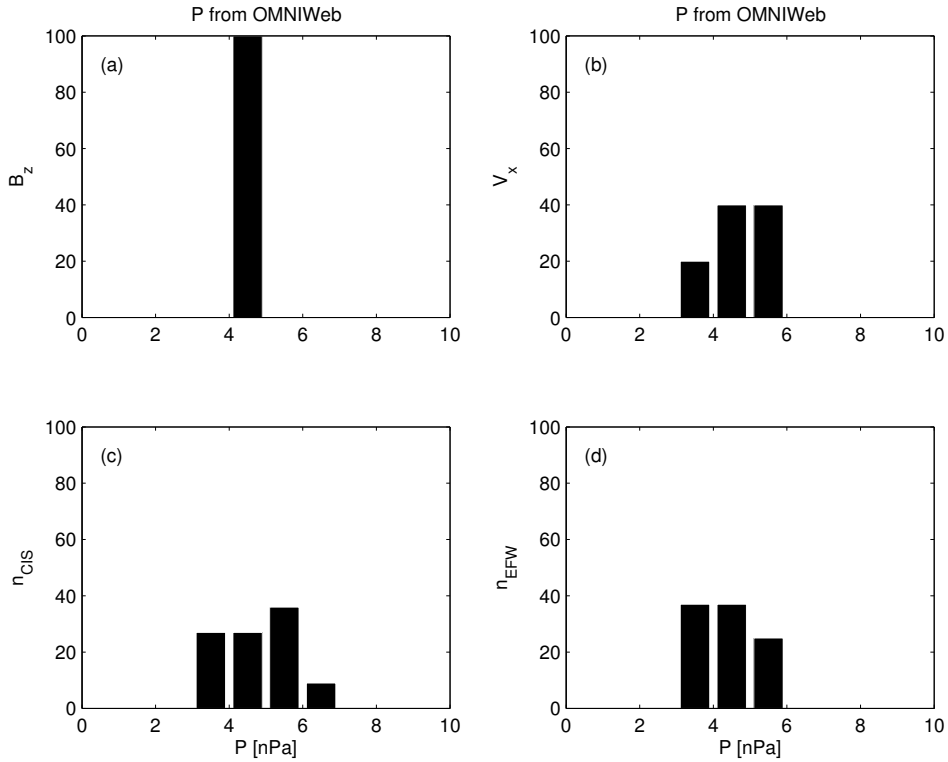
921 **Figure 14.** (a, b, c) The distributions of the OMNI solar wind magnetic field (B_x , B_y , B_z)
 922 components, (d, e, f) the OMNI solar wind velocity (V_x , V_y , V_z) components and (g) the solar
 923 wind dynamic pressure during the 1-year run from January 29, 2002 to February 2, 2003 in GSE
 924 reference frame, respectively. The relative values are given on the vertical axis of all plots in
 925 percentage.



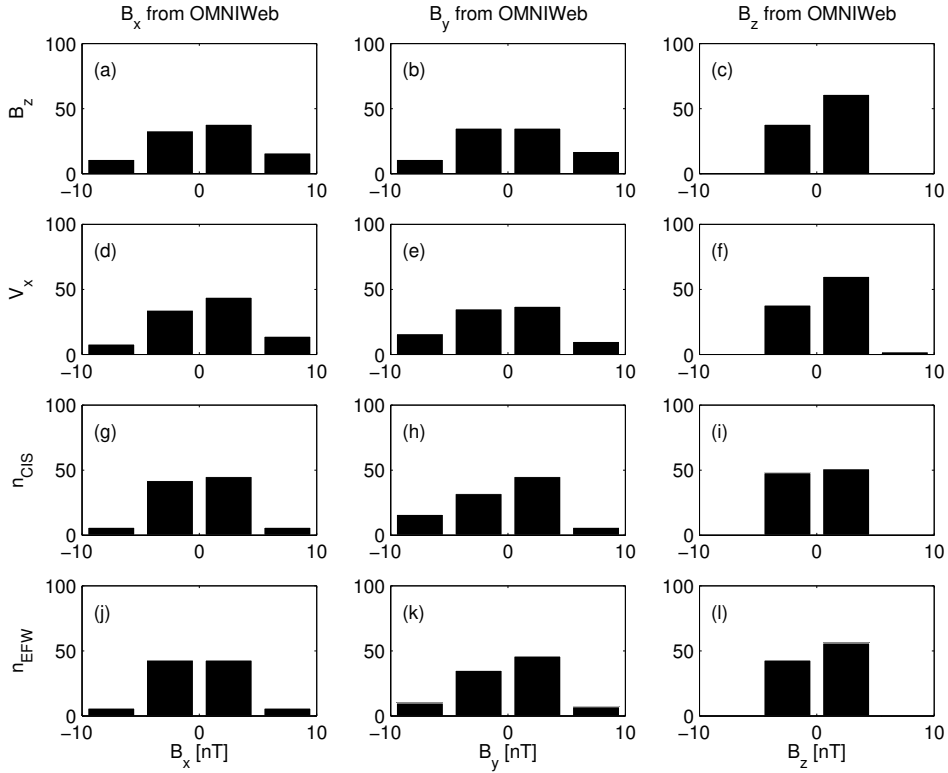
926 **Figure 15.** The distributions of the B_x , the B_y and the B_z OMNI solar wind magnetic field
 927 components when the agreement of the Cluster SC3 measurements and the GUMICS–4 simu-
 928 lations are poor in the solar wind (see Table 4). The B_z , the V_x , the n_{CIS} and the n_{EFW} are
 929 the magnetic field GSE Z component, the plasma ion velocity X GSE component, the solar wind
 930 density measured by the CIS HIA instrument and the calculated from the EFW spacecraft po-
 931 tential, respectively. (a, b, c) Distribution of OMNI B_x , B_y , B_z when the agreement of B_z is
 932 poor. (d, e, f) Distribution of OMNI B_x , B_y , B_z when the agreement of V_x is poor. (g, h, i)
 933 Distribution of OMNI B_x , B_y , B_z when the agreement of n_{CIS} is poor. (j, k, l) Distribution of
 934 OMNI B_x , B_y , B_z when the agreement of n_{EFW} is poor. The values are in percentage unit in
 935 the distributions.



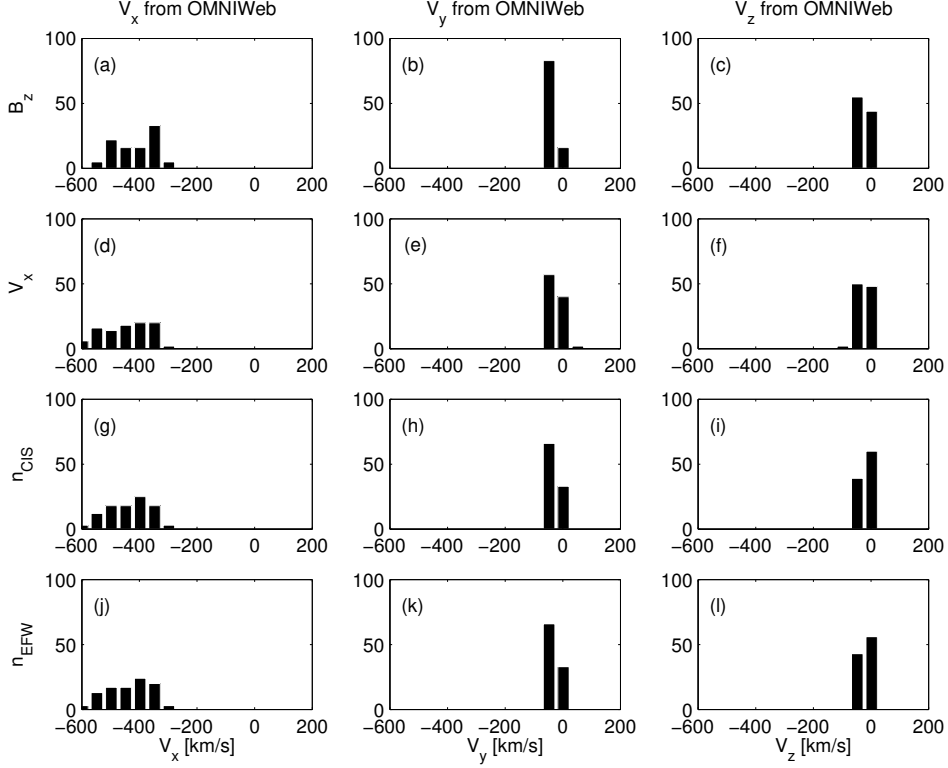
936 **Figure 16.** The distributions of the V_x , the V_y and the V_z OMNI solar wind magnetic field
 937 components when the agreement of the Cluster SC3 measurements and the GUMICS–4 simu-
 938 lations are poor in the solar wind (see Table 4). The B_z , the V_x , the n_{CIS} and the n_{EFW} are
 939 the magnetic field GSE Z component, the plasma ion velocity X GSE component, the solar wind
 940 density measured by the CIS HIA instrument and the calculated from the EFW spacecraft po-
 941 tential, respectively. (a, b, c) Distribution of OMNI V_x , V_y , V_z when the agreement of B_z is poor.
 942 (d, e, f) Distribution of OMNI V_x , V_y , V_z when the agreement of V_x is poor. (g, h, i) Distribution
 943 of OMNI V_x , V_y , V_z when the agreement of n_{CIS} is poor. (j, k, l) Distribution of OMNI V_x , V_y ,
 944 V_z when the agreement of n_{EFW} is poor. The values are in percentage unit in the distributions.



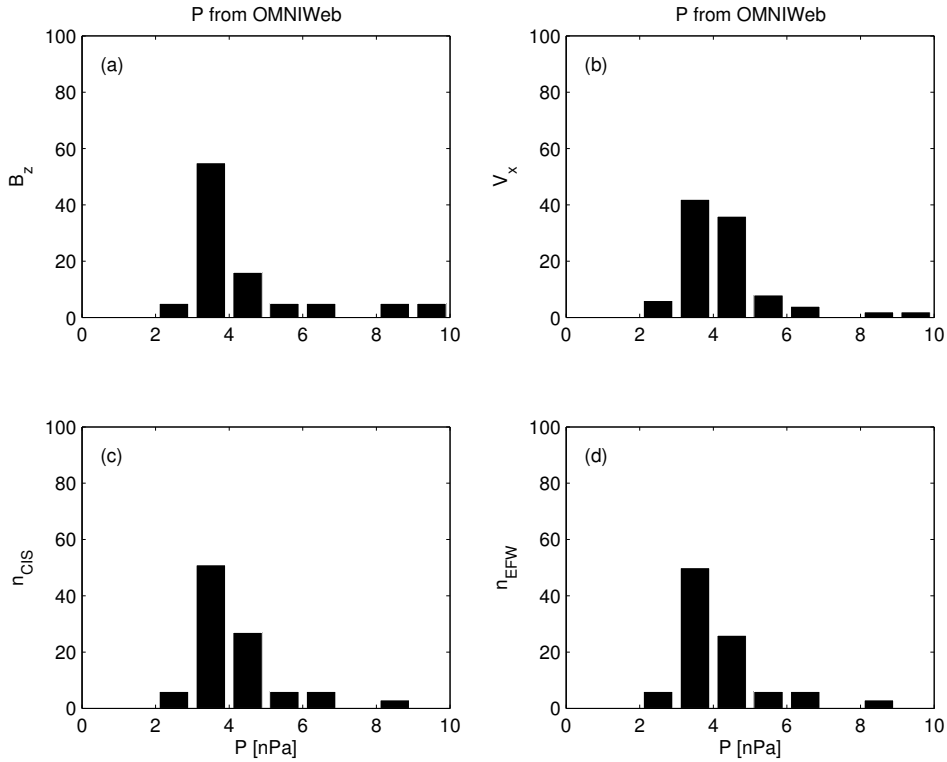
945 **Figure 17.** The distributions of the P solar wind dynamic pressure calculated from OMNI
 946 parameters when the agreement of the Cluster SC3 measurements and the GUMICS–4 simula-
 947 tions are poor in the solar wind (see Table 4). The B_z , V_x , n_{CIS} and n_{EFW} are the magnetic
 948 field GSE Z component, the velocity X GSE component, the solar wind density measured by the
 949 CIS HIA instrument and calculated from the EFW spacecraft potential, respectively. (a, b, c, d)
 950 The distribution of the P calculated from OMNI data when the agreement of the B_z , the V_x , the
 951 n_{CIS} or the n_{EFW} are poor. The values are in percentage unit in the distributions.



952 **Figure 18.** The distributions of the B_x , the B_y and the B_z OMNI solar wind magnetic field
953 components when the agreement of the Cluster SC3 measurements and the GUMICS–4 simu-
954 lations are poor in the magnetosheath (see Table 5). The B_z , the V_x , the n_{CIS} and the n_{EFW}
955 are the magnetic field GSE Z component, the plasma ion velocity X GSE component, the solar
956 wind density measured by the CIS HIA instrument and the calculated from the EFW spacecraf-
957 t potential, respectively. (a, b, c) Distribution of OMNI B_x , B_y , B_z when the agreement of B_z
958 is poor. (d, e, f) Distribution of OMNI B_x , B_y , B_z when the agreement of V_x is poor. (g, h, i)
959 Distribution of OMNI B_x , B_y , B_z when the agreement of n_{CIS} is poor. (j, k, l) Distribution of
960 OMNI B_x , B_y , B_z when the agreement of n_{EFW} is poor. The values are in percentage unit in
961 the distributions.



962 **Figure 19.** The distributions of the V_x , the V_y and the V_z OMNI solar wind magnetic field
963 components when the agreement of the Cluster SC3 measurements and the GUMICS–4 simula-
964 tions are poor in the magnetosheath (see Table 5). The B_z , the V_x , the n_{CIS} and the n_{EFW} are
965 the magnetic field GSE Z component, the plasma ion velocity X GSE component, the solar wind
966 density measured by the CIS HIA instrument and the calculated from the EFW spacecraft po-
967 tential, respectively. (a, b, c) Distribution of OMNI V_x , V_y , V_z when the agreement of B_z is poor.
968 (d, e, f) Distribution of OMNI V_x , V_y , V_z when the agreement of V_x is poor. (g, h, i) Distribution
969 of OMNI V_x , V_y , V_z when the agreement of n_{CIS} is poor. (j, k, l) Distribution of OMNI V_x , V_y ,
970 V_z when the agreement of n_{EFW} is poor. The values are in percentage unit in the distributions.



971 **Figure 20.** The distributions of the P solar wind dynamic pressure calculated from OMNI pa-
 972 rameters when the agreement of the Cluster SC3 measurements and the GUMICS-4 simulations
 973 are poor in the magnetosheath (see Table 5). The B_z , V_x , n_{CIS} and n_{EFW} are the magnetic
 974 field GSE Z component, the velocity X GSE component, the solar wind density measured by the
 975 CIS HIA instrument and calculated from the EFW spacecraft potential, respectively. (a, b, c, d)
 976 The distribution of the P calculated from OMNI data when the agreement of the B_z , the V_x , the
 977 n_{CIS} or the n_{EFW} are poor. The values are in percentage unit in the distributions.

Start/End	C_{B_z}	δt_{B_z}	C_{V_x}	δt_{V_x}	$C_{n_{CIS}}$	$\delta t_{n_{CIS}}$	$C_{n_{EFW}}$	$\delta t_{n_{EFW}}$
	[min]		[min]		[min]		[min]	
20020201 20:00/0203 04:00	0.96	2	1.00	13	0.96	3	0.98	3
20020211 13:00/0212 12:00	0.82	2	1.00	0	0.99	18	0.99	18
20020218 09:00/0219 02:00	0.93	0	1.00	-3	0.94	-3	0.97	-3
20020219 06:30/0219 15:00	0.93	1	1.00	0	0.99	-60	1.00	-52
20020220 18:30/0222 00:00	0.87	4	1.00	4	0.93	-21	0.98	3
20020318 17:30/0319 02:30	0.89	1	1.00	21	0.98	50	0.99	5
20020412 20:30/0413 02:00	0.90	4	0.99	-54	0.94	60	0.98	12
20021227 12:00/1228 03:00	0.75	4	1.00	-3	0.99	-26	0.99	21
20021229 20:00/1230 16:00	0.68	1	1.00	1	0.99	-30	0.98	41
20030106 06:00/0106 19:00	0.79	4	1.00	6	0.99	4	0.99	-60
20030108 07:00/0109 03:30	0.55	10	1.00	41	0.99	10	0.97	-55
20030113 08:30/0113 18:00	0.91	3	1.00	5	1.00	3	0.97	-1
20030120 07:30/0120 13:00	0.82	2	1.00	9	1.00	-6	1.00	-3
20030122 12:00/0123 14:00	0.81	2	1.00	3	0.99	3	0.92	-60
20030124 18:00/0126 00:00	0.73	3	1.00	0	0.99	-60	0.99	60
20030127 16:00/0128 06:00	0.88	-1	1.00	-3	0.95	1	0.88	11
20030129 12:00/0130 18:00	0.90	2	1.00	4	0.94	-59	0.98	1

978 **Table 1.** The studied solar wind intervals. The correlation coefficients (C_{B_z} , C_{V_x} , $C_{n_{CIS}}$,
979 $C_{n_{EFW}}$) and time shift (δt_{V_x} , $\delta t_{n_{CIS}}$, $\delta t_{n_{EFW}}$) in minutes of the magnetic field GSE Z compo-
980 nent (B_z), solar wind velocity X component (V_x), CIS and EFW densities (n_{CIS} , n_{EFW}).

Table 2: The studied magnetosheath intervals. The correlation coefficients (C_{B_z} , C_{V_x} , $C_{n_{CIS}}$, $C_{n_{EFW}}$) and time shift (δt_{V_x} , $\delta t_{n_{CIS}}$, $\delta t_{n_{EFW}}$) in minutes of the magnetic field GSE Z component (B_z), solar wind velocity X component (V_x), CIS and EFW densities (n_{CIS} , n_{EFW}). In the empty slots the correlation calculation gives invalid result.

Start/End	C_{B_z}	δt_{B_z}	C_{V_x}	δt_{V_x}	$C_{n_{CIS}}$	$\delta t_{n_{CIS}}$	$C_{n_{EFW}}$	$\delta t_{n_{EFW}}$
		[min]		[min]		[min]		[min]
20020201 13:30/0201 18:30	0.91	1	0.98	56	0.99	60	0.976	60
20020208 18:15/0209 00:00	0.73	2	0.95	60	0.98	-52	0.98	-54
20020211 02:30/0211 09:00	0.79	0	0.99	-20	0.99	-1	0.99	1
20020212 16:30/0212 21:00	0.80	3	0.99	54	0.99	31	0.99	30
20020219 17:30/0219 23:00	0.76	4	0.98	37	0.99	7	0.99	6
20020222 23:00/0223 06:30	0.64	0	0.97	-60	0.99	-47	0.98	-48
20020227 16:30/0227 23:15	0.48	59	0.98	-31	0.99	-39	1.00	-12
20020310 18:30/0311 00:30	0.97	3	0.98	19	0.99	8	0.99	-2
20020311 14:00/0311 19:00	0.86	5	0.97	36	0.99	-3	0.99	-40
20020406 19:00/0407 01:15	0.76	2	0.96	-60	0.98	-55	0.98	-56
20020410 17:30/0410 23:00	0.89	6	0.99	-50	0.99	3	1.00	5
20020411 11:30/0411 16:30	0.82	4	0.99	39	0.99	3	0.99	3
20020418 18:30/0418 22:45	0.92	60	0.99	-60	0.99	60	0.98	60
20020421 04:30/0421 07:45	0.96	47	0.99	-60	1.00	-60	1.00	-60
20020422 11:45/0422 15:45	0.73	-5	0.98	-17	0.99	-15	0.98	-16
20020423 08:30/0423 12:30	0.93	31	0.99	3	0.99	16	0.99	16
20020430 12:30/0430 17:00	0.79	59	0.98	22	0.98	-18		
20020505 07:00/0505 11:15	0.71	59	0.99	-58	0.98	-60		
20020506 19:15/0507 00:15	0.84	-27	0.98	-60	0.97	-37		
20020507 17:30/0507 23:00	0.93	2	0.98	-30	0.99	-49		
20020514 22:45/0515 03:00	0.79	49	0.99	35	0.99	38	0.99	43
20020517 07:00/0517 12:15	0.74	-5	1.00	-5	0.99	-4	0.99	-3
20020518 13:30/0518 19:30	0.70	1	0.99	9	0.97	-1	0.97	-1

Continued on next page

Table 2 – *Continued from previous page*

Start/End	C_{B_z}	δt_{B_z}	C_{V_x}	δt_{V_x}	$C_{n_{CIS}}$	$\delta t_{n_{CIS}}$	$C_{n_{EFW}}$	$\delta t_{n_{EFW}}$
		[min]		[min]		[min]		[min]
20020519 20:00/0520 03:30	0.98	2	1.00	-9	0.99	-5	0.99	-50
20020520 10:45/0520 20:15	0.77	1	0.99	-3	0.95	-1	0.99	-1
20020522 02:00/0522 08:45	0.49	52	0.99	4	0.99	12	0.99	22
20020527 02:15/0527 17:15	0.79	-3	0.99	-3	0.98	0	0.98	0
20020530 05:00/0530 10:30	0.29	3	1.00	-38	0.99	3	0.99	3
20020601 19:30/0602 01:00	0.68	-2	1.00	18	0.99	-6	0.99	-7
20020602 21:45/0603 17:45	0.62	-5	0.99	-1	0.98	2	0.99	2
20020605 10:30/0606 06:00	0.18	0	1.00	-7	0.97	10	0.98	9
20020607 18:00/0607 22:00	0.92	-35	1.00	-36	0.99	16	0.99	16
20020608 01:15/0608 18:15	0.53	-4	0.99	-39	0.96	-6	0.97	-6
20020610 01:30/0610 09:30	0.76	5	0.99	8	0.99	-5	0.99	-7
20020610 11:00/0611 01:00	0.87	-4	0.99	-33	0.98	23	0.99	6
20020612 18:30/0613 06:15	0.44	-2	0.99	-7	0.97	4	0.97	-32
20020615 07:00/0615 23:30			1.00	47	0.98	-3	0.98	-3
20020617 05:00/0618 03:45	0.76	4	1.00	28	0.98	10	0.98	8
20020620 04:00/0620 11:00	0.61	-8	0.99	-6	0.97	12	0.98	4
20020622 14:30/0622 18:00	0.98	55	1.00	35	0.99	16	1.00	16
20021201 04:15/1202 07:45	0.38	1	1.00	2	0.99	6	0.99	6
20021203 15:30/1204 19:30	0.67	1	0.99	60	0.98	59	0.98	59
20021207 00:30/1207 07:45	0.49	37	0.98	-56	0.99	-19	0.99	-4
20021208 09:30/1209 08:00	0.69	2	0.98	-35	0.97	6	0.98	4
20021212 23:30/1213 14:30	0.51	5	1.00	36	0.99	-3	0.81	-56
20021213 21:15/1214 09:30	0.93	5	0.99	-35	0.99	-13	0.99	-47
20021215 12:45/1216 18:00	0.76	2	0.99	-60	0.94	-60	0.98	31
20021217 16:30/1218 01:45	0.99	2	1.00	-54	0.99	3	0.99	3
20021220 01:30/1220 06:15	0.92	0	1.00	60	0.99	2	0.99	3
20021223 02:15/1223 13:00	0.91	1	0.97	49	0.93	49	0.99	-14
20021223 14:00/1223 22:30	0.84	1	0.99	-2	0.99	-1	1.00	-3
20021224 19:00/1225 01:45	0.94	0	1.00	-44	0.99	26	0.99	27

Continued on next page

Table 2 – *Continued from previous page*

Start/End	C_{B_z}	δt_{B_z}	C_{V_x}	δt_{V_x}	$C_{n_{CIS}}$	$\delta t_{n_{CIS}}$	$C_{n_{EFW}}$	$\delta t_{n_{EFW}}$
		[min]		[min]		[min]		[min]
20021225 23:45/1226 07:15	0.96	7	1.00	-17	0.99	56	0.99	55
20021226 23:00/1227 09:45	0.79	2	1.00	2	0.98	4	0.99	3
20021229 11:45/1229 17:00	0.60	2	1.00	-60	0.98	-19	0.98	50
20021230 17:45/1231 01:00	0.69	1	0.98	52	0.98	60	0.98	22
20021231 23:00/0101 05:15	0.89	2	0.99	15	0.99	-54	1.00	-58
20030105 14:00/0105 21:00	0.69	0	0.99	1	0.98	-60	0.99	-60
20030106 23:15/0107 03:00	0.52	9	0.98	60	0.99	56	1.00	-60
20030109 08:45/0109 16:15			0.91	-56	0.98	-13	0.98	-26
20030110 07:15/0110 15:15	0.94	1	0.99	-7	0.99	1	0.98	5
20030111 08:15/0111 22:30	0.84	0	0.99	-59	0.94	-15	0.94	8
20030112 17:30/0113 00:15	0.98	0	1.00	-52	0.99	39	0.99	51
20030114 00:30/0114 08:30	0.84	-1	0.99	-60	0.98	23	0.98	8
20030116 10:15/0116 17:45	0.62	60	0.93	52	0.99	60	0.99	30
20030117 09:30/0117 13:30	0.68	-3	1.00	8	1.00	-31	0.99	-33
20030118 23:30/0119 03:45	0.93	3	1.00	-12	1.00	7	0.99	7
20030119 21:00/0120 01:00	0.94	3	1.00	5	1.00	38	1.00	19
20030121 06:30/0121 11:30	0.82	-15	0.96	47	0.98	7	0.99	-39
20030122 04:45/0122 09:30	0.69	-2	1.00	10	0.99	-9	0.99	-5
20030126 01:45/0126 06:30	0.85	3	0.99	-15	0.99	-50	0.99	23
20030127 08:15/0127 13:00	1.00	9	1.00	-60	0.98	0	0.99	1
20030128 12:30/0128 17:15	0.77	60	0.99	-24	0.99	-6	0.988	20
20030130 19:45/0131 00:15	0.98	2	0.99	51	0.99	25	0.99	9

Table 3: The studied magnetosphere intervals (UT).

Start/End
20020213 23:00/0214 01:30
20020217 18:30/0218 02:00
20020220 00:45/0220 12:00
20020222 11:15/0222 20:15
20020225 02:15/0225 08:30
20020227 06:00/0227 12:00
20020302 00:00/0302 03:15
20020306 10:00/0306 18:30
20020308 17:30/0309 06:00
20020311 02:15/0311 12:00
20020313 11:15/0314 00:15
20020316 04:45/0316 08:00
20020318 09:00/0318 14:45
20020320 20:30/0320 23:55
20020323 04:00/0323 09:45
20020327 23:45/0328 06:15
20020330 07:15/0330 12:45
20020401 19:30/0401 22:00
20020406 09:30/0406 18:00
20020408 15:00/0409 00:00
20020410 23:30/0411 09:45
20020413 08:30/0413 19:00
20020416 18:00/0417 04:30
20020418 06:00/0418 12:00
20020420 15:00/0420 23:00
20020422 20:00/0423 07:00
20020425 08:30/0425 18:00
20020430 04:40/0430 12:00
20020504 14:30/0504 16:45

Continued on next page

Table 3 – *Continued from previous page*

Start/End
20020505 02:30/0505 07:00
20020507 01:30/0507 15:45
20020508 11:00/0510 04:15
20020512 02:45/0512 09:30
20020514 10:30/0514 12:45
20020519 00:30/0519 19:30
20020521 01:30/0521 22:00
20020523 23:30/0524 02:00
20020524 19:00/0525 08:15
20020526 07:30/0526 10:30
20020528 20:00/0529 05:00
20020531 02:15/0531 13:30
20020602 04:30/0602 07:30
20020602 12:00/0602 21:30
20020604 08:30/0605 07:00
20020606 14:30/0607 16:30
20020609 06:00/0609 20:00
20020611 11:00/0612 13:00
20020614 01:00/0614 16:00
20020616 08:00/0616 18:00
20020620 13:30/0622 01:00
20020623 13:00/0623 17:00
20020624 04:00/0624 10:15
20020630 17:45/0701 15:00
20020701 21:00/0703 10:30
20020703 23:00/0706 03:15
20020707 01:00/0708 23:00
20020710 11:30/0714 03:30
20020714 15:45/0715 15:30
20020716 23:30/0717 16:00

Continued on next page

Table 3 – *Continued from previous page*

Start/End
20020718 05:45/0722 11:00
20020722 23:45/0728 01:00
20020728 02:00/0804 03:45
20020804 04:45/0811 06:15
20020811 07:30/0816 01:00
20020816 15:30/0818 09:00
20020818 10:00/0825 11:30
20020825 13:00/0901 14:15
20020901 17:15/0903 23:30
20020905 02:15/0906 16:30
20020907 10:30/0908 17:00
20020908 18:00/0915 19:30
20020915 21:00/0922 22:30
20020923 00:00/0923 23:30
20020924 03:30/0928 22:45
20020928 23:30/0930 01:00
20020930 02:15/1006 17:00
20021006 17:45/1007 03:30
20021007 05:00/1007 17:30
20021008 07:30/1010 22:00
20021010 22:30/1012 22:30
20021012 23:00/1014 06:30
20021014 09:00/1016 04:00
20021016 14:00/1019 00:15
20021019 01:30/1019 22:00
20021021 04:00/1022 19:30
20021022 22:30/1026 02:30
20021026 04:00/1029 20:15
20021030 01:30/1102 08:00
20021102 22:00/1104 22:00

Continued on next page

Table 3 – *Continued from previous page*

Start/End
20021106 00:00/1107 18:00
20021108 02:00/1109 18:45
20021111 00:00/1112 01:30
20021113 03:45/1114 14:15
20021115 20:30/1116 23:00
20021118 01:00/1118 23:30
20021120 17:00/1121 06:00
20021122 21:30/1124 01:00
20021125 04:00/1126 08:30
20021127 20:00/1128 18:30
20021130 04:00/1201 01:30
20021202 14:30/1203 09:00
20021204 22:00/1205 19:30
20021207 09:00/1207 16:30
20021207 18:00/1207 22:00
20021209 16:30/1210 14:30
20021212 13:45/1212 21:30
20021214 13:30/1214 20:00
20021214 21:00/1215 07:30
20021216 21:00/1217 15:00
20021219 08:00/1219 19:30
20021221 15:45/1221 23:15
20021222 00:30/1222 08:45
20021224 02:30/1224 14:00
20021226 10:00/1226 19:00
20021228 19:30/1229 02:30
20021229 04:00/1229 10:00
20021231 05:00/1231 18:45
20030102 12:30/0102 20:45
20030104 20:45/0105 06:00

Continued on next page

Table 3 – *Continued from previous page*

Start/End
20030105 07:00/0105 13:30
20030107 05:45/0107 21:00
20030109 17:00/0110 00:45
20030112 00:00/0112 09:15
20030112 10:30/0112 16:00
20030114 11:00/0114 20:00
20030116 20:30/0116 22:45
20030119 04:30/0119 09:30
20030119 14:00/0119 17:00
20030121 13:30/0121 21:30
20030126 07:30/0126 15:45
20030128 17:45/0129 08:15
20030131 01:30/0131 11:45

Start/End	OMNI			Cluster SC3			
	B_z [nT]	V_x [km/s]	P [cm $^{-3}$]	B_z	V_x	n_{CIS}	n_{EFW}
20020201 20:00/0203 04:00	-1.25	-373.52	4.08	y	y	n	y
20020211 13:00/0212 12:00	0.03	-533.11	2.18	y	y	y	y
20020218 09:00/0219 02:00	2.56	-362.41	3.46	y	n	n	y
20020219 06:30/0219 15:00	3.55	-401.63	1.25	y	y	n	n
20020220 18:30/0222 00:00	1.95	-440.18	1.96	y	y	n	y
20020318 17:30/0319 02:30	3.79	-429.30	15.34	y	n	n	n
20020412 20:30/0413 02:00	-1.81	-420.35	3.24	y	n	n	y
20021227 12:00/1228 03:00	0.09	-714.40	2.72	y	n	n	y
20021229 20:00/1230 16:00	-0.37	-526.40	2.26	y	y	n	n
20030106 06:00/0106 19:00	2.25	-399.91	1.50	y	n	n	n
20030108 07:00/0109 03:30	-0.58	-280.80	2.97	n	n	y	n
20030113 08:30/0113 18:00	0.68	-397.83	1.72	y	y	y	n
20030120 07:30/0120 13:00	2.16	-630.69	2.43	y	y	y	y
20030122 12:00/0123 14:00	0.13	-608.96	3.41	y	y	y	n
20030124 18:00/0126 00:00	-0.71	-739.68	2.87	y	y	n	n
20030127 16:00/0128 06:00	-0.92	-451.84	3.12	y	y	n	n
20030129 12:00/0130 18:00	-3.09	-450.00	3.96	y	y	n	y

983 **Table 4.** The average OMNI input parameters in the solar wind and the good/bad agreement
 984 of the GUMICS–4 simulations to the Cluster B_z magnetic field component, the V_x solar wind
 985 speed component, the n_{CIS} solar wind density measured by the Cluster CIS HIA instrument and
 986 the n_{EFW} solar wind density calculated from the spacecraft potential measured by the Cluster
 987 EFW instrument in the solar wind.

Table 5: The average OMNI input parameters in the solar wind and the good/bad agreement of the GUMICS–4 simulations to the Cluster B_z magnetic field component, the V_x solar wind speed component, the n_{CIS} solar wind density measured by the Cluster CIS HIA instrument and the n_{EFW} solar wind density calculated from the spacecraft potential measured by the Cluster EFW instrument in the magnetosheath.

Start/End	OMNI			Cluster SC3			
	B_z	V_x	P	B_z	V_x	n_{CIS}	n_{EFW}
	[nT]	[km/s]	[cm $^{-3}$]				
20020201 13:30/0201 18:30	0.19	-342.87	4.62	y	n	n	n
20020208 18:15/0209 00:00	-0.48	-508.16	1.61	y	n	n	n
20020211 02:30/0211 09:00	-1.85	-425.67	1.78	y	y	y	y
20020212 16:30/0212 21:00	2.98	-509.22	2.34	y	n	n	n
20020219 17:30/0219 23:00	1.46	-431.50	1.46	y	y	y	y
20020222 23:00/0223 06:30	0.86	-391.22	1.14	y	n	n	n
20020227 16:30/0227 23:15	1.89	-343.13	1.52	n	n	n	n
20020310 18:30/0311 00:30	-2.81	-379.46	1.78	y	y	y	y
20020311 14:00/0311 19:00	1.63	-371.43	2.68	n	n	n	n
20020406 19:00/0407 01:15	-2.71	-333.13	0.93	y	n	n	n
20020410 17:30/0410 23:00	0.31	-312.43	4.42	n	n	y	y
20020411 11:30/0411 16:30	-1.50	-494.02	4.25	y	y	n	n
20020418 18:30/0418 22:45	-0.92	-450.82	0.30	n	n	n	n
20020421 04:30/0421 07:45	0.40	-455.69	1.37	n	n	n	n
20020422 11:45/0422 15:45	0.25	-419.98	1.14	n	n	y	y
20020423 08:30/0423 12:30	2.77	-507.99	6.82	n	n	n	n
20020430 12:30/0430 17:00	2.15	-479.51	3.02	n	n	n	n
20020505 07:00/0505 11:15	0.20	-336.81	1.74	n	n	n	n
20020506 19:15/0507 00:15	0.78	-390.00	2.46	y	n	n	n
20020507 17:30/0507 23:00	2.87	-392.40	3.49	y	n	n	n
20020514 22:45/0515 03:00	-2.42	-414.01	1.82	n	n	n	n

Continued on next page

Table 5 – *Continued from previous page*

Start/End	OMNI			Cluster SC3			
	B_z [nT]	V_x [km/s]	P $[cm^{-3}]$	B_z	V_x	n_{CIS}	n_{EFW}
20020517 07:00/0517 12:15	-0.39	-379.32	1.52	y	y	y	y
20020518 13:30/0518 19:30	0.63	-345.87	1.59	n	n	y	y
20020519 20:00/0520 03:30	4.75	-408.56	1.12	y	y	y	y
20020520 10:45/0520 20:15	0.74	-448.89	1.93	y	y	y	y
20020522 02:00/0522 08:45	-1.07	-398.12	1.63	n	y	y	y
20020527 02:15/0527 17:15	-3.11	-542.53	2.07	y	y	y	y
20020530 05:00/0530 10:30	0.03	-493.86	2.08	y	n	y	y
20020601 19:30/0602 01:00	-3.38	-342.27	4.16	y	y	y	y
20020602 21:45/0603 17:45	0.38	-435.47	1.89	y	y	y	y
20020605 10:30/0606 06:00	-0.42	-394.49	1.08	y	y	n	n
20020607 18:00/0607 22:00	-1.60	-291.85	1.80	y	y	y	y
20020608 01:15/0608 18:15	0.06	-335.39	2.74	y	n	y	y
20020610 01:30/0610 09:30	1.60	-465.52	3.00	y	y	y	y
20020610 11:00/0611 01:00	-2.27	-419.86	2.16	y	n	y	y
20020612 18:30/0613 06:15	-1.13	-351.03	1.16	y	y	y	y
20020615 07:00/0615 23:30	-1.16	-334.27	2.84	n	n	y	y
20020617 05:00/0618 03:45	0.78	-351.47	1.87	y	n	y	y
20020620 04:00/0620 11:00	0.46	-485.48	1.73	y	y	y	y
20020622 14:30/0622 18:00	-0.72	-429.02	1.93	n	n	y	y
20021201 04:15/1202 07:45	-1.09	-499.23	2.62	y	y	y	y
20021203 15:30/1204 19:30	0.34	-449.09	2.06	y	n	n	n
20021207 00:30/1207 07:45	0.80	-451.80	7.33	n	n	y	y
20021208 09:30/1209 08:00	0.60	-600.27	1.49	y	n	y	y
20021212 23:30/1213 14:30	0.10	-337.77	1.32	y	n	n	n
20021213 21:15/1214 09:30	-0.74	-361.19	2.99	y	n	y	y
20021215 12:45/1216 18:00	1.32	-479.48	1.53	y	n	n	n
20021217 16:30/1218 01:45	4.56	-393.99	2.49	y	n	y	y
20021220 01:30/1220 06:15	-1.21	-530.62	3.01	y	n	y	y

Continued on next page

Table 5 – *Continued from previous page*

Start/End	OMNI			Cluster SC3			
	B_z [nT]	V_x [km/s]	P $[cm^{-3}]$	B_z	V_x	n_{CIS}	n_{EFW}
20021223 02:15/1223 13:00	-2.32	-516.12	2.22	y	n	n	n
20021223 14:00/1223 22:30	0.89	-519.77	2.55	y	y	y	y
20021224 19:00/1225 01:45	0.88	-523.86	3.41	y	n	y	y
20021225 23:45/1226 07:15	-0.61	-414.38	2.21	y	y	n	n
20021226 23:00/1227 09:45	-1.79	-618.14	6.20	y	y	y	y
20021229 11:45/1229 17:00	-0.41	-580.12	2.39	y	n	n	n
20021230 17:45/1231 01:00	-1.01	-483.60	1.93	y	n	n	y
20021231 23:00/0101 05:15	0.60	-418.95	1.94	y	n	n	n
20030105 14:00/0105 21:00	-0.03	-414.46	1.69	y	n	n	n
20030106 23:15/0107 03:00	-1.62	-392.29	1.56	n	n	n	n
20030109 08:45/0109 16:15	1.45	-272.82	2.31	n	n	n	n
20030110 07:15/0110 15:15	-2.11	-401.03	2.72	y	n	y	y
20030111 08:15/0111 22:30	-0.20	-433.33	1.24	y	n	n	y
20030112 17:30/0113 00:15	1.53	-389.62	1.45	y	n	n	n
20030114 00:30/0114 08:30	-1.67	-388.53	2.27	y	n	n	y
20030116 10:15/0116 17:45	-1.20	-328.91	1.22	n	n	n	n
20030117 09:30/0117 13:30	-1.36	-327.09	2.55	y	y	y	y
20030118 23:30/0119 03:45	6.41	-459.46	4.82	y	y	y	y
20030119 21:00/0120 01:00	1.52	-597.95	2.38	y	n	y	y
20030121 06:30/0121 11:30	-1.77	-670.25	1.50	y	n	n	n
20030122 04:45/0122 09:30	0.11	-588.87	2.30	y	n	y	y
20030126 01:45/0126 06:30	-0.24	-713.82	2.75	y	y	y	y
20030127 08:15/0127 13:00	7.94	-509.30	0.47	y	n	y	y
20030128 12:30/0128 17:15	4.95	-443.83	4.15	y	y	y	y
20030130 19:45/0131 00:15	4.21	-510.33	2.63	y	n	y	y

Start/End	GUMICS Neutral Sheet
20020901 19:10/0901 23:54	–
20020906 14:07/0906 16:37	+
20020913 17:33/0913 20:06	+
20020918 12:47/0918 14:26	–
20020920 20:36/0921 02:13	+
20020928 02:58/0928 07:00	+
20021002 16:12/1002 23:52	–
20021014 12:34/1014 22:53	+
20021017 03:08/1017 04:11	–

989 **Table 6.** Intervals around the studied neutral sheet crossings in the tail. The Cluster SC3
 990 crossed the neutral sheet in all cases. The 3rd column shows whether the neutral sheet is visible
 991 in the GUMICS–4 simulations.